Mechanism of gating and partial agonist action in the glycine receptor

Jie Yu[1,5], Hongtao Zhu[1,5], Remigijus Lape[3], Timo Greiner[3], Juan Du[1,4], Wei Lü[1,4], Lucia Sivilotti[3,7], Eric Gouaux[1,2,6,7]

1. Vollum Institute, Oregon Health & Science University, Portland, Oregon 97239, USA.

2. Howard Hughes Medical Institute, Oregon Health & Science University, Portland, Oregon 97239, USA.

3. Department of Neuroscience, Physiology and Pharmacology, University College London, Medical Sciences Building, Gower Street, London WC1E 6BT, UK.

4. Present address: Van Andel Institute, 333 Bostwick Ave. NE, Grand Rapids, MI 49503, USA.

5. These authors contributed equally.

6. Lead contact

7. Correspondence to Lucia Sivilotti: l.sivilotti@ucl.ac.uk or Eric Gouaux: gouauxe@ohsu.edu

Summary

Ligand-gated ion channels mediate signal transduction at chemical synapses and transition between resting, open and desensitized states in response to neurotransmitter binding. Neurotransmitters that produce maximum open channel probabilities (Po) are full agonists whereas those that yield lower than maximum Po are partial agonists. Cys-loop receptors are an important class of neurotransmitter receptors yet a structure-based understanding of the mechanism of partial agonist action has proven elusive. Here we study the glycine receptor with the full agonist glycine and the partial agonists taurine and γ-amino butyric acid. We use electrophysiology to show how partial agonists populate agonist-bound, closed channel states, and cryo-EM reconstructions to illuminate the structures of intermediate, pre-open states, providing insights into previously unseen conformational states along the receptor reaction pathway. We further correlate agonist-induced conformational changes to Po across members of the receptor family, providing a hypothetical mechanism for partial and full agonist action at Cys-loop receptors.

Keywords

ligand-gated ion channels; partial agonists action; glycine receptor; gating mechanism; cryo-EM; SMA

Introduction

Agonists can differ in their efficacy and produce different maximum responses on the same receptors (Colquhoun, 1998). “Partial agonists”, a term coined by Stephenson in 1956 (Stephenson, 1956), display submaximal efficacy. Early work on the muscle nicotinic acetylcholine receptor (nAChR) (Del Castillo and Katz, 1957), a Cys-loop or pentameric ligand-gated channel (pLGIC), led to the hypothesis that efficacy is determined by the agonist’s ability to keep the channel open after it has bound. In pLGICs, agonist efficacy is reflected in the maximum open probability seen in single-channel recordings when the channel is fully occupied by the agonist yet is not desensitized. Neurotransmitters are often full agonists (Burzomato et al., 2004; Colquhoun and Sakmann, 1985), but partial agonists are of interest for therapeutics and include varenicline (Lam and Patel, 2007), a partial agonist of neuronal nAChR. In the auditory system, GABA, a partial agonist of glycine receptors (GlyRs), is co-released with glycine and both agonists act on the GlyR to sculpt the time course of postsynaptic responses (Lu et al., 2008). pLGICs are also important therapeutic targets and include the neuronal and muscle nAChR, $GABA_A$ receptors ($GABA_AR$) and 5-HT_3 receptors (5-HT_3R) (Changeux and Edelstein, 1998).

GlyRs are an outstanding vehicle for investigating the mechanism of agonist efficacy. Studies by Katz and Thesleff outlined the canonical gating mechanism of pLGICs as the transition from closed/resting, open/activated and closed/desensitized states (Katz and Thesleff, 1957). Recent electrophysiological studies of GlyRs, however, showed that channel activation is not a simple isomerization from resting to open states, but rather involves a landscape of one or more pre-open intermediates (Auerbach, 2005; Burzomato et al., 2004; Lape et al., 2012). The presence of multiple agonist-bound closed states is a general feature of pLGICs, where the closed intermediate states have increased affinity for the agonist (Corradi et al., 2009; Jadey and Auerbach, 2012; Lape et al., 2008; Mukhtasimova et al., 2009). Fitting models that include activation intermediates to pLGIC single channel data has led to the proposal that the limited efficacy of partial agonists is due to their reduced ability to change the channel conformation to a

short-lived pre-open intermediate (flipped/primed), rather than the reduced ability to open the receptor once the intermediate is reached (Corradi and Bouzat, 2014; Lape et al., 2008; Mukhtasimova et al., 2016).

Here we investigate the structural basis of partial agonist activation in GlyR, exploiting extensive functional characterization showing that taurine and GABA act as partial agonists (Fucile et al., 1999; Schmieden et al., 1992, 1993). While previous GlyR structures have shed light on the mechanism of full agonist, antagonist and modulator action (Du et al., 2015; Huang et al., 2015; Huang et al., 2017a; Huang et al., 2017b; Kumar et al., 2020), structures of the receptor bound to partial agonists are absent. Furthermore, the previously solved structures employed the receptor in detergent micelles as well as constructs lacking the M3/M4 cytoplasmic loop, factors that likely underlie the physiologically irrelevant 'super open' state of the ion channel pore and the anomalously high Po of the receptor constructs (Cerdan et al., 2018; Du et al., 2015; Gonzalez-Gutierrez et al., 2017). Recently, a cryo-EM structure of the glycine-bound, picrotoxin-blocked state of full length GlyR was elucidated (Kumar et al., 2020), where the receptor was reconstituted, together with soy bean lipids, into nanodiscs (Ritchie et al., 2009). This study provides insight into the full agonist-bound state of the receptor, but the blocking of the channel with picrotoxin yields an ion channel in a non conductive state.

To address the question of partial agonist action and to elucidate structures of the receptor in native, lipidic environment, we isolated the full length (FL) GlyR using the stryrene maleic acid polymer (SMA), enabling direct extraction of the receptor as a complex with endogenous lipids (Dorr et al., 2016; Knowles et al., 2009). We further reconstituted FL receptors into nanodiscs with brain lipids, and we then determined high resolution structures of the receptor bound to glycine, taurine or GABA in both the SMA and nanodisc environments. We explored both the SMA and nanodisc strategies because they both allow for the envelopment of the receptor transmembrane domain with native or native-like lipids (Dorr et al., 2016; Knowles et al., 2009; Ritchie et al., 2009),

recognizing the sensitivity of membrane proteins (Autzen et al., 2019; Jamshad et al., 2011) and pLGICs to their membrane or membrane-mimic environment (Baenziger et al., 2015; Heidmann et al., 1980). These studies of GlyR bound to taurine or GABA reveal, for the first time, agonist-bound closed states as well as open and desensitized states, illuminating conformational states along the receptor reaction pathway and providing structure-based insights into the mechanism of partial-agonist action.

Results and Discussion

Glycine-bound complex populates multiple states

Glycine is a full agonist and single-channel analysis of clusters of receptor activity, excluding the long-lived desensitized states, reveals a maximum open probability (P_O) of 97% (Figure 1A). Macroscopic current recordings elicited by saturating glycine show that the current decays to 57 ± 8% (*n*=8) of peak after 1s application because of desensitization (Figure S1A). Thus, under steady state conditions the glycine-bound receptor populates both open and desensitized states. To elucidate the structures of these states, we extracted the receptor using SMA or reconstituted the receptor into nanodiscs (Supplemental Information) and prepared cryo-EM grids in the presence of 10 mM glycine. Single particle cryo-EM studies of glycine-bound receptor in nanodiscs revealed a single closed desensitized or desensitized-like state (Figures S1C-S1D and S2, Table S1), which is at odds with electrophysiology data that shows the receptor populates both of open and desensitized states in the presence of glycine. We reasoned that either the lipids or perhaps the nanodisc complex itself shifts the conformational equilibrium of the receptor to the desensitized state and thus pursued studies of the receptor-SMA complex.

Single particle cryo-EM studies of the GlyR-SMA-gly complex revealed open (GlyR-SMA-gly-open), desensitized (GlyR-SMA-gly-desensitized) and expanded-open (GlyR-SMA-gly-expanded-open) states with overall resolutions of 2.9 Å, 3.1 Å and 4.0 Å, respectively (Figure 1B-1F, Figures S2-S3 and Tables S2). Importantly, these reconstructions have well resolved

transmembrane domain (TMD) densities, especially for the M2 helices, allowing us to locate the 9'L and -2'P residues, thus informing the definition of functional state. In all of the structures the ion channel pores are open at 9'L but adopt three distinct conformations at the -2'P position (Figure 1G-1I).

The three conformations at the -2'P position represent open, desensitized and expanded-open states. In the GlyR-SMA-gly-open state the constriction of the pore is ~5.6 Å, in agreement with the pore diameter ~5.3 Å estimated from functional studies and sufficient to allow permeation of partially hydrated chloride ions (Hille, 2001) and block by cyanotriphenylborate (Rundstrom et al., 1994) (Figure 1C, 1G). The GlyR-SMA-gly-desensitized state has a constriction at -2'P of 3 Å in diameter, indicative of a non-conducting state (Figure 1C, 1H). In the GlyR-SMA-gly-expanded-open state the pore has a minimum diameter of ~7 Å at -2'P, a dimension that is larger than that estimated by electrophysiological sizing experiments (Lynch, 2004) but smaller than that of the truncated receptor in detergent micelles ($GlyR_{EM}$-micelle-gly; PDB code: 3JAE) (Du et al., 2015) (Figure 1C, 1I, Figures S1E and S4A). To further assess the variable 'open state' pore diameters determined from structural studies (Du et al., 2015), we note that propionate, with an effective diameter of ~5.2 Å (Bormann et al., 1987), is one of the largest permeant organic anions. Isethionate, with an unhydrated diameter of ~6.2 Å (Sunesen et al., 2006), is an organic anion slightly larger than propionate and is impermeant in pLGIC anionic channels (Schwartz and Yu, 1995). Because the expanded-open state has a minimum diameter of 7 Å, and thus should be large enough to conduct isethionate, we suggest that the expanded-open state is too large to be the physiologically relevant open state. Thus, in addition to an expanded open state, the SMA-solubilized receptor yields conformations in physiologically relevant open and desensitized states, suggesting that SMA-extracted GlyR particles may provide insights into structure-based mechanisms of receptor function.

Partial agonist bound states

Single-channel recordings of GlyR in the presence of 100 mM taurine or GABA feature long-lived shut states while the channel is not desensitized, suggesting the presence of additional partial agonist-bound shut states (Figure 2A). Indeed, the maximum P_O for taurine and GABA is 66 ± 3% and 39 ± 3%, respectively, substantially lower than that of glycine (98 ± 1%; 71, 83 and 83 clusters from 5-11 patches; mean ± SEM) (Figure 1A). The partial agonists are also less potent, with effective concentrations (EC_{50}) for taurine and GABA of 1.05 ± 0.08 mM and 28.4 ± 0.9 mM, respectively (cf. glycine: 190 ± 20 µM; Figure 2C). In the subsequent structural studies, we applied 20 mM taurine and 40 mM GABA to the receptor prior to grid preparation for both the nanodisc and SMA data sets (Figures S5 and S7-S8, Supplementary information). The concentration of GABA employed for grid preparation was limited by its solubility and at higher concentrations GABA precipitated, rendering imaging the grids impossible.

Analysis of the partial agonist data sets reveals four 3D classes (Figures S6-S8, Tables S2-S3), with 3 of the taurine- or GABA-bound structures similar to the glycine-bound open, desensitized, and expanded-open states (Figure 2D-2K, Figure S4B-S4C). Importantly, we discovered a fourth, previously unseen, partial agonist-bound closed conformation of the receptor. There is clear density for the partial agonists in the neurotransmitter binding pocket (Figure S4E-S4H) and the M2 helices are oriented approximately perpendicular to the membrane, creating a constriction less than 3 Å in diameter at 9'L and rendering the channel impermeable to Cl^- (Figure 2F, 2I, 2J, 2K). At the -2'P site, the pore has a diameter of 4 Å, intermediate between the open and desensitized states.

We hypothesize that the closed state, partial agonist-bound cryo-EM structures provide the first visualization of the additional long-lived shut states that are seen in single-channel recordings with partial agonists (Figure 2A). These states are not seen with glycine (Figure 1A) because, by contrast, the glycine-bound closed conformation of the receptor is short-lived, as the receptor rapidly and nearly completely transitions to the brief intermediate "flipped" state (Lape et al., 2008), precluding its capture by single-particle cryo-EM. In comparison to glycine, taurine or

GABA's reduced ability to 'flip' GlyR, as well as their propensity to promote the receptor's return from the flipped state to the closed state, allows us to capture agonist-bound closed states via cryo-EM. We suggest that the cryo-EM partial agonist-bound closed states most likely represent unflipped states. The particle fractions of the open or desensitized states are smaller for taurine as compared with glycine, and are smaller still for GABA. Conversely, the fraction of particles in the closed state is highest for the GABA dataset, lower for the taurine dataset, and absent in the glycine dataset (Figure 2B).

Neurotransmitter binding site

In all complexes, the densities for glycine, taurine and GABA are well defined, enabling positioning of the agonists in the neurotransmitter binding site (Figure 3A-3C). In the glycine complex, the agonist's amino and carboxyl groups form multiple hydrogen bonding interactions and a cation-π contact (Figure 3D), consistent with the GlyR-α3 crystal structure (Huang et al., 2017b). While the orientations of taurine and GABA are similar to that of glycine, the interactions between the amino groups of the agonists and receptor residues are different (Figure 3E-3F) yet, as in the glycine complex, the sulfate group of taurine and the carboxylate group of GABA participate in multiple hydrogen bonds.

To identify the changes in the binding pocket upon agonist binding, we solved the structure of the apo/resting state in detergent micelles (apo-$GlyR_{EM}$; Figure S9, Table S4-S5). The apo-$GlyR_{EM}$ structure has a pore constriction at 9'L, consistent with the apo-GluCl (Althoff et al., 2014), apo-GlyR in nanodisc (Kumar et al., 2020) and the taurine/GABA-bound GlyR closed states (Figure S1H). Comparison of the apo/resting state conformation of the agonist binding pocket with the open state/agonist-bound complexes shows that the binding pocket undergoes a 'contraction' where loop C transitions from an "uncapped" to "capped" configuration and loop B moves towards to the agonist (Figure 3I), as hypothesized for the muscle nicotinic acetylcholine receptor (Celie et al., 2004; Jadey and Auerbach, 2012; Mukhtasimova et al., 2009; Tripathy et al., 2019).

The extent of binding pocket contraction, however, is different between full and partial agonists, with the volume of the agonist binding pocket smallest in the glycine-bound structure (Hansen et al., 2005). Thr220 in loop C, Phe175 in loop B, Arg81 in β2, and Ser145 in β6 all coordinate taurine and GABA in a manner that is similar, yet slightly different than their coordination of glycine. In the glycine complex, Cα atoms of residues in loop C and in loop B 'contract' toward the agonist compared with the taurine-bound pocket (Figure 3G, 3H). We propose that these conformational changes are coupled to agonist-induced activation (Lynch, 2004), consistent with the notion that the agonist causes increased stabilization of the activated configuration (Changeux, 2012) . Thus, in the full agonist-bound open state, loops B and C move closer to the ligand in comparison to partial agonists, resulting in a smaller binding pocket and a more efficient activation of the receptor (Figure 3H). Our structural data, together with agonist-dependent measurements on the nAChR, 5HT-3 and GABA receptor, show that full and partial agonist complexes of the open state of a pLGIC, within the confines of the agonist-binding site, are not identical and that full agonists yield a more 'compact' binding site in comparison to partial agonists. Indeed, the ligand volumes and distances spanning the binding site ($D_{F175\text{-}S145}$ and $D_{T220\text{-}R81}$) are correlated with agonist efficacy (Table S6).

GABA acts on YGF mutant with a high Po

To test if the degree of contraction of the agonist binding pocket by partial agonists is correlated to agonist efficacy, we investigated the F175Y/Y177F variant (YGF) (Schmieden et al., 1993). Remarkably, on the YGF mutant GABA is an almost full agonist, with a Po of 92 ± 2% (*n*=18 clusters, Figure 4B) and is more potent in activating the channel or displacing strychnine (Figure 4A, 4C). Glycine remains a full agonist (Po of ~1.0; Figure 4A) and taurine has a Po of 95 ± 5% (*n*=26 clusters). We proceeded to solve the cryo-EM structure of the SMA-solubilized YGF mutant bound with GABA, obtaining high-resolution maps for the open, desensitized and expanded-open states (Figure 4H, Figures S4D, S9 and Table S4). We did not observe any 3D classes associated with the closed state seen for partial agonists in FL GlyRs (Figure S10A).

The increased binding affinity of GABA to the YGF mutant arises from additional interactions involving the carboxylate group of GABA, including a hydrogen bond with the hydroxyl oxygen of Tyr175 (Figure 4D). Superposition of the binding pockets of the FL and YGF mutant highlights other differences between interactions of receptor side chains. The mutation of Tyr177 to Phe disrupts the hydrogen bond formed with Trp110 through the hydroxyl oxygen of Tyr177, whereas the mutation of Phe175 to Tyr yields an additional hydrogen bond with Ser145 (Figure 4E). These interactions enable loop B to move closer to the (-) subunit, reducing the binding pocket volume similar to that of the FL glycine open complex (Figure 4F, 4G), thus supporting the notion that contraction of the agonist binding pocket is correlated to agonist efficacy (Table S6).

To understand why GABA is almost a full agonist at the $GABA_AR$ but a partial agonist for GlyR, we also superimposed the binding pocket of GlyR with the canonical GABA binding site of the $GABA_AR$ (Mortensen et al., 2004; Phulera et al., 2018). Remarkably, most of the residues coordinating GABA in the two receptors are identical (Figure S10B-S10C). Moreover, the binding pocket of the GlyR open state has a smaller volume than GABA-bound $GABA_AR$ (Figure S10D), implying that the opening of $GABA_AR$ requires a smaller contraction of the binding pocket to fully transition the receptor to the open state. To explore if the simple substitution of the three tyrosine residues of $GABA_AR$ with the phenylalanine residues of GlyR enables GABA to act as a full agonist on the GlyR, we prepared the YYY mutant (F115Y/F175Y/F223Y) and found that GABA remained a weak partial agonist, with a similar Po in the YYY mutant as in the FL receptor (Figure S10E). Thus, the tuning of agonist efficacy requires precise changes in the pocket volume and in agonist-receptor interactions that go beyond which residues interact directly with the agonist (Mukhtasimova and Sine, 2018).

Partial agonists produce distinct ECD and ECD-TMD conformational changes

To understand the conformational changes associated with transition from the closed-to-open states, we used the well resolved, SMA-solubilized taurine-bound structures. Upon the closed-to-open transition, loop B and loop C move towards the agonist (Figure 5A, 5C, 5F) and

residues in β6 and β2 shift away from the (+) subunit. Transduction of the conformational changes from the agonist binding pocket to the ECD-TMD interfaces include the repositioning of the β8-β9 loop by loop C and loop B, reshaping of β1-β2 loop by β2, reseating of the Cys-loop by β6 and loop B, and movement of pre-M1 by loop C (Figure 5E and Figure S1B). The M2-M3 loop acts as a "bridge", forming contacts with the ECD and repositioning the M2 and M3 helices. From the taurine-closed to the taurine-open state, the M2-M3 loop moves away from the ion channel pore (Figure 5G). Pro291, positioned beneath Thr70, stabilizes the M2 and M3 helices in the taurine-open state, reminiscent of the position of Val45 and Pro268 in the GluCl in complex with ivermectin (Hibbs and Gouaux, 2011). Furthermore, in the taurine-closed state, the Ser294 to Gln235 hydrogen bond is ruptured during receptor activation, facilitating the outward movement of the M2 helix (Figure 5E, 5G). This action agrees with reports that the mutation of Ser294 to cysteine increases glycine EC50 by ~5 fold (Lynch et al., 2001).

Comparison of the taurine-open to the taurine-desensitized state shows that the binding pockets and the ECD-TMD interfaces adopt the same conformation (Figure 5A, 5B, 5D). The transition from open to desensitized states thus involves local interactions in the ion permeation pathway (Auerbach and Akk, 1998; Plested, 2016), with desensitization proceeding from an uncoupling between the ECD and TMD (Zhang et al., 2013). In the ECD-TMD interfaces, a hydrogen bond between Gln235 and Gln202 stabilizes the receptor in the open and desensitized states (Figure 5D). Consistent with our results, ablation of this interaction, such as in the *shaky* startle mouse, reduces glycine potency (Janzen et al., 2017). While the overall conformational changes of the GABA and taurine structures are similar (Figure S11), in the taurine-closed state, the loop B and loop C are closer to the agonist, compared with the GABA-closed state (Figure S12F-S12H), providing structural insights into the differences between GABA and taurine in inducing the hypothetical flipped state of kinetic models, with the assumption that the taurine and GABA-bound closed states are not already flipped.

In comparison to pLGICs in closed/resting states (Basak et al., 2018; Du et al., 2015; Hilf and Dutzler, 2008; Huang et al., 2015; Miyazawa et al., 2003), the taurine-closed states illustrate how agonist binding promotes local rearrangements at the neurotransmitter binding site, prior to the overall changes associated with channel opening (Figure S12A-S12E and Figure S13). In the taurine-closed state, loop C is in a "capped" configuration as compared with the apo-$GlyR_{EM}$ and apo 5-$HT_{3A}R$ structures, due to the binding of agonist (Figure S12B). By contrast, the ECD-TMD interfaces of the two structures are similar, with identical conformations for M2-M3, β1-β2, β8-β9 and Cys loops (Figure S12D), showing that local movements of loop C alone cannot induce substantial conformational changes that affect the receptor ECD-TMD interfaces as well as the TMDs. The 5-$HT_{3A}R$ ECD-TMD interface shows substantial differences compared with the taurine/GABA-closed state (Figure S12C-S12E), indicating the contraction of the binding pocket around the agonist and the induced changes in the ECD-TMD interface are unique for each pLGIC.

Conformational changes of the ion channel pore

In the transition from the closed to the open states, the TMD of each subunit undergoes a counterclockwise rotation of ~8.6 °, expanding the pore and opening the ion channel, allowing for Cl^- permeation (Figure 5A, 5I, 5J and Figure S12I). Within the M1-M4 helices, the M2 helices have a more pronounced movement, with a rotation of ~13°. During the transition from the open to the desensitized state, the major conformational changes are in the TMD, with each subunit undergoing a clockwise rotation by ~2° (Figure S12J). The lower half of the pore is occluded at -2'P, moving by ~1.4 Å, in agreement with observations in the homomeric GlyR and $GABA_A$ receptor, and the α4β2 nicotinic receptor in the desensitized state (Kumar et al., 2020; Laverty et al., 2019; Masiulis et al., 2019; Walsh et al., 2018) (Figure 5A, 5H, 5J). In this process, the M2 helix exhibits a larger motion, with an inward rotation of ~3°. The M1-M2 loop undergoes a relatively large displacement during desensitization, in agreement with studies showing that mutation of the M1-M2 loop affects entry into desensitization (Breitinger et al., 2004; Gielen et al., 2015).

Partial agonist gating mechanism

We have captured partial agonist-bound closed states, which we hypothesize are poised between the resting and the open/desensitized states, thus enabling visualization of intermediate or preopen-shut states of the ion channel, in accord with partial agonist-bound, long-lived shut states in the single-channel recordings (Figure 2A). Binding of a partial agonist induces a contraction in the binding pocket, yet to a lesser extent than the full agonist (Figure 6A-6C). These ECD changes promote the receptor transition from closed-to-open, in which the TMD undergoes an outward rotation and expands the channel pore at the -2'P and 9'L positions (Figure 6C). Sustained binding of agonist promotes a further transition into the desensitized state, involving an inward rotation of the TMD and occlusion of the pore at -2'P (Figure 6D). Because of the structural diversity of ligands and the complexity of functional behavior of each pLGIC, the precise details of the contraction of the binding site may be specific to each subgroup of the superfamily. Nevertheless, we hypothesize that the agonist-bound closed, open and desensitized states link efficacy to the contraction of the agonist binding site, thus providing a speculative structural proposal for partial agonist gating of GlyR and of pLGICs as a whole.

Acknowledgements

We thank L. Vaskalis for assistance with figures, F. Jalali-Yazdi for discussion and Polyscope for the SMA. Electron microscopy was performed at OHSU at the Multiscale Microscopy Core. This work was supported by MRC grant MR/R009074/1 to L.G.S. and NIH grant R01 GM100400 to E.G.. E.G. is an investigator of the Howard Hughes Medical Institute.

Author contributions

J.Y., H.Z. and E.G. designed the project. J.Y. performed the sample preparation for cryo-EM and biochemistry studies. J.Y. and H.Z. performed the cryo-EM data collection. H.Z. and J.Y. analyzed the data. H.Z. performed the model building and ligand binding assay. J.D. and W.L. performed the cryo-EM data collection and processing for apo-GlyR_{EM}. T.G., R.L. and L.G.S. performed the electrophysiological experiments and wrote the related method section. All authors wrote and edited the manuscript.

Declaration of Interests

The authors declare no competing interests.

Main Figure Legends

Figure 1. Single channel electrophysiology and cryo-EM analysis of the glycine complex.

A. Single-channel recording of GlyR openings in the presence of 10 mM glycine.

B. Fractions of GlyR particles in the desensitized, open and expanded/super-open states in nanodiscs, SMA, or detergent micelles. Error bars represent SEM, as described in the Methods.

C. Plots of pore radius for glycine-bound states. The Cα position of Arg 268 (M2 0') is set to 0.

D-F. Cryo-EM density maps. The partially transparent surface represents lipid-SMA density.

G-I. Ion permeation pathways where M2 helices of two subunits are shown in ribbon and the side chains of pore-lining residues are shown in sticks, calculated by the program HOLE (radii coloring: red <1.8 Å, green 1.8–3.3 Å, and blue > 3.3 Å).

See also Figures S1-S3 and Tables S1-S2, S5, S7.

Figure 2. Partial agonist complexes probed by electrophysiology and cryo-EM.

A. Representative cell-attached single-channel recordings of GlyR openings elicited by 100 mM taurine and 100 mM GABA, respectively.

B. Fractions of GlyR particles in the open, closed, desensitized and expanded-open states of the glycine, taurine and GABA complexes of the SMA-solubilized receptor, calculated by RELION and cisTEM as described in the Methods. Error bars represent SEM.

C. Whole cell, dose-response data for glycine, taurine and GABA. EC_{50} for glycine, taurine and GABA are 190 ± 20 μM, 1050 ± 80 μM and 28.4 ± 0.9 mM, respectively. Error bars represent SEM and $n \geqslant 6$ cells for all experiments. Curves are normalized to the glycine maximum current recorded in each cell.

D-F. Distances (in angstrom) and conformation of residues -2'P and 9'L in the taurine-bound, SMA-solubilized receptor in the open, desensitized and closed states.

G-I. Ion permeation pathway for taurine-bound states, calculated using HOLE and plotted as in Figure 1.

J-K. Pore radius as a function of distance along the pore axis for taurine-bound states (**J**) and GABA-bound states (**K**) of the SMA-solubilized receptor.

See also Figures S1, S3-S8 and Tables S1-S3, S5, S7.

Figure 3. **Neurotransmitter binding sites.**

A-C. Illustration of the densities for glycine, taurine and GABA, contoured at 11 σ, 10 σ, and 8 σ, respectively. For the neurotransmitters, carbon and sulfate atoms are colored in black, whereas nitrogen and oxygen atoms are in blue and red, respectively.

D-F Glycine, taurine and GABA binding sites showing hydrogen bonds and cation-π interactions as dashed lines.

G. Illustration of conformational changes produced by the binding of glycine, taurine and GABA by superimposing the respective extracellular domains (ECDs).

H. Schematic diagram illustrating the changes in distances (angstrom) of key residues for the glycine, taurine and GABA-bound open states. The glycine, taurine and GABA structures are green, gray and pink, respectively.

I. Conformational changes of the binding pockets in the apo state, glycine-bound open, taurine-bound open and taurine-bound closed states by superimposing the main chain atoms of the ECDs.

See also Figures S10, S12 and Table S6.

Figure 4. YGF mutation renders GABA a high efficacy agonist.

A. Whole cell, dose response data for glycine and GABA for full length (FL) or the YGF mutant. EC_{50} for glycine at FL and YGF mutant are 190 ± 20 μM and 33 ± 3 μM, respectively. EC_{50} for GABA to FL and YGF mutant are 28.4 ± 0.9 mM and 1.05 ± 0.08 mM, respectively. Error bars represent SEM and $n \geqslant 6$ cells for all experiments. Responses are normalized to maximum responses to glycine in each cell.

B. Cell-attached single-channel recording showing openings of the YGF mutant produced by 100 mM GABA.

C. Competition ligand binding experiment using ^{3}H-strychnine. Data are shown as means ± SEM (n=3). Ki of GABA to FL and YGF mutant are 1.41 ± 0.94 mM and 0.18 ± 0.07 mM, respectively. Kd of ^{3}H-strychnine in the FL and YGF mutant are 220 ± 3 nM and 54 ± 4 nM, respectively.

D. GABA binding site in the YGF mutant viewed parallel to the membrane (left) or from the extracellular side of the membrane (right). GABA density is contoured at 0.013 σ. The possible hydrogen bonds and cation-π interactions are shown as dashed lines.

E. Superimposition of the binding pockets from the FL and YGF mutant in the presence of GABA to show the impact on the binding pocket of the swap between Y177 and F175.

F. Conformational changes in the binding pockets of the open states of GABA-bound YGF mutant and FL and glycine-bound FL shown by superposing the ECDs.

G. Schematic diagram illustrating changes in the distances in the binding pocket of the GABA-bound YGF mutant (blue) and FL (pink) as well as glycine-bound FL (green).

H. Plots for pore radius as a function of distance along the pore axis for GABA-bound YGF mutant in the open, desensitized and expanded-open states.

See also Figures S9-S10 and Table S4.

Figure 5. **Conformational changes between the open, desensitized and closed states.**

A. Structure of the taurine-open state. Two subunits are shown in cartoon and the other three subunits are represented as partially transparent surfaces. Taurine is in sphere representation. The binding pocket in the ECD, the ECD-TMD interface and the TMD are indicated by a black solid, a black dashed and a purple solid rectangle, respectively.

B-G. Superposition of the (-) subunit illustrates the relative movements in the (+) subunit. Hydrogen bonds are shown in dashed lines. The taurine-open, taurine-desensitized and taurine-closed states are colored in yellow, salmon and cyan, respectively. (**B. D**) Comparison of the

binding pocket (**B**) and ECD-TMD interfaces (**D**) between taurine-open and taurine-desensitized states. (C. E) Conformational changes in the binding pockets (**C**) and the ECD-TMD interfaces (**F**) between taurine-closed, taurine-open states. (**F. G**) Illustration of the changes in distances of the Cα atoms of key residues in the binding pockets (**F**) and ECD-TMD interfaces (**G**) between taurine-open and taurine-closed states. Cα atoms in the taurine-open and taurine-closed states are represented by yellow and blue balls, respectively.

H-I. Superimposition of a single subunit illuminates the changes in the TMD between taurine-closed, taurine-open and taurine-desensitized states. The M1, M3 and M4 helices are shown as cylinders while the M2 helix is shown in cartoon representation.

J. The plot of the differences in the position of Cα atoms from residues in the M2 helix derived from the taurine-open, taurine-desensitized and taurine-closed states. Two constriction sites are indicated by dash lines. From open to desensitized states, the major changes are concentrated at the lower half of the M2 helix with -2'P moving by 1.4 Å. By contrast, the M2 helix undergoes a larger conformational change upon transition from the closed to open states.

See also Figures S11-S13.

Figure 6. GlyR gating mechanism.

The ECD changes promote the transition from closed to the open state (**A-C**), while sustained binding of partial agonist promotes a further transition into the desensitized state (**C-D**).

Supplemental Figure Legends

Figure S1 Cryo-EM studies on the GlyR reconstituted into nanodisc. Related to Figures 1 and 2.

A. Macroscopic responses of GlyR to the rapid application of 10 mM glycine, 100 mM taurine and 100 mM GABA to the same outside-out patch. In this patch the agonist current left at the end of the 1-s pulse was 17% for glycine (cf. average of 57±8%, range 17-89%, 8 patches).

B. A single subunit of the glycine-bound open state of GlyR viewed parallel to the membrane with secondary structure elements and key loops labeled.

C. Cryo-EM reconstruction map of GlyR complexed with glycine in the nanodisc environment, viewed parallel to the membrane (GlyR-nanodisc-gly). One subunit is highlighted in green. The nanodisc density is indicated with a partially transparent blue surface.

D-E. Ion permeation pathways for GlyR-nanodisc-gly (green) and $GlyR_{EM}$-micelle-gly (grey, PDB code: 3JAE). The M2 helices of two subunits are shown in ribbon and the side chains of pore-lining residues are shown in sticks representation. As calculated by the program HOLE, different colors define different radii: red <1.8 Å, green 1.8–3.3 Å, and blue > 3.3 Å.

F-G. Conformational differences in the M2 helices between the desensitized and closed states of GlyR complexed with taurine (F) and GABA (G) in nanodiscs. The residues at two constrictions, 9'L and -2'P, are shown as sticks.

H. Plots of pore radius as a function of distance along the pore axis for desensitized and closed states of GlyR complexed with taurine and GABA in nanodiscs as well as the apo-$GlyR_{EM}$ structure determined in a detergent micelle.

Figure S2 3D reconstructions for glycine-bound states in nanodiscs (green box) and SMA (blue box). Related to Figure 1.

A. SEC trace for GlyR in the nanodisc and SDS-PAGE analysis of peak fractions.

B. A typical cryo-EM micrograph for the glycine-bound GlyR - nanodisc complex.

C. Selected 2D class averages.

D. Local resolution estimate of the unsharpened map.

E. FSC plots before (unmasked) and after (masked) RELION post processing, and between the model and the final map.

F. Particle angular distribution.

G. SEC trace for glycine-bound GlyR in SMA and SDS-PAGE analysis of the peak fraction.

H. Typical cryo-EM micrograph.

I. Selected 2D class averages.

J. M and P. Local resolution estimation of unsharpened open, desensitized and expanded-open maps, respectively.

K. **N and Q**. FSC curves before (unmasked) and after (masked) RELION post processing, and between the model and the final maps for open, desensitized and expanded-open states, respectively.

l. **O and R**. Particle angular distributions for open, desensitized and expanded-open maps, respectively.

Figure S3 Representative densities of the glycine or taurine complex maps. Related to Figures1 and 2.

The structures are shown in stick and maps are in mesh. For each panel, the M1 and M2 helices together with the M1-M2 loop starting from Y239 to S286 are isolated, contoured at 6.5 σ to 8 σ. In the nanodisc maps, a density feature of a putative lipid molecule has been modeled as an alkane chain. The M2-M3 loop from A288 to Y295 is illustrated, contoured at 6.5 σ to 8 σ. The β2 strand of the ECD from residue D73 to W84 is isolated, contoured at 7.5 σ to 8 σ. The maps associated with the nanodisc and SMA reconstructions were sharpened by RELION and Localscale, respectively.

Figure S4. Representative cryo-EM densities of the M2 helices in the expanded-open states and of the partial agonists in the closed states. Related to Figure 2.

A-D. Cryo-EM densities and models for the pore lining M2 helices in the expanded-open states of GlyR or YGF mutant complexes solved using receptor isolated in SMA, showing the protruding densities at the intracellular end of M2 helices. The origin of these extra densities is unknown

because of the low resolution, thus making them difficult to model. The constriction site at the -2'P position is indicated.

E-H. GABA densities in the nanodisc (**E**) and SMA (**F**) complexes are contoured at 3 σ and 4 σ, respectively. Taurine densities in the nanodisc (**G**) and SMA (**H**) complexes are contoured at 4 σ and 0.02 σ, respectively.

Figure S5 Data processing flow chart for the taurine-bound GlyR complex in nanodiscs. Related to Figure 2 and STAR Methods.

Figure S6 Data processing flow chart for the taurine-bound GlyR isolated using SMA. Related to Figure 2 and STAR Methods.

Figure S7 3D reconstructions for taurine-bound states in nanodiscs (green box) and SMA (blue box). Related to Figure 2.

A. A typical cryo-EM micrograph of the taurine-bound nanodisc complex. Scale bar represents the size of 30 nm.

B. Selected 2D class averages.

C and E. Local resolution maps for unsharpened taurine bound desensitized and closed states, respectively.

D and F. FSC curves before (unmasked) and after (masked) RELION post processing, and between the model and the final map.

G. A typical cryo-EM micrograph of the taurine-bound SMA complex. . Scale bar represents the size of 30 nm.

H. Selected 2D class averages.

I. K. M and O. Local resolution maps for unsharpened open, desensitized, closed and expanded-open states, respectively.

J. L. N and P. FSC curves before (unmasked) and after (masked) RELION post processing, and between the model and the final map for open, desensitized, closed and expanded-open maps, respectively.

Figure S8 3D reconstructions for GABA-bound states in the nanodisc (green box) and SMA (blue box). Related to Figure 2.

A. A typical cryo-EM micrograph for GABA-bound GlyR in nanodiscs. . Scale bar represents the size of 30 nm.

B. Selected 2D class averages.

C and E. Unsharpened local resolution maps for the GABA-bound desensitized and closed states, respectively.

D and F. FSC curves before (unmasked) and after (masked) RELION post processing, and between the model and the final map for GABA-bound GlyR at desensitized and closed states, respectively.

G. A typical cryo-EM micrograph for taurine-bound GlyR in SMA. . Scale bar represents the size of 100 nm.

H. Selected 2D class averages.

I. K. M and **O**. Local resolution maps for unsharpened open, desensitized, closed and expanded-open, respectively.

J. L. **N** and **P.** FSC curves before (unmasked) and after (masked) RELION post processing, and between the model and the final map for open, desensitized, closed and expanded-open, respectively.

Figure S9 3D reconstructions for the GABA-bound states of the YGF mutant in SMA and the apo state of $GlyR_{EM}$ in detergent micelles. Related to Figure 4.

A. A typical cryo-EM micrograph. . Scale bar represents the size of 100 nm.

B. Selected 2D class averages.

C. E and G. Local resolution maps for unsharpened open, desensitized and expanded-open states.

D. F and H. FSC curves before (unmasked) and after (masked) RELION post processing, and between the model and the final map for open, desensitized and expanded-open states, respectively.

J. A typical cryo-EM micrograph. . Scale bar represents the size of 20 nm.

K. Selected 2D class averages.

L. M. Local resolution map and FSC plot for the apo-$GlyR_{EM}$ reconstruction.

Figure S10 Fraction of GlyR particles of different states in the full length (FL) and YGF mutant and differences in the binding pocket between GlyR and α1β1γ2 GABA receptor-GABA complex ($GABA_AR$, PDB code: 6DW1). Related to Figures 3 and 4.

A. Fractions of GlyR particles in different states in the FL and YGF mutant, calculated by RELION and cisTEM. Error bars represent SEM

B. Reference model for the extracellular domain (ECD) of the open state of the GlyR complex with GABA in the SMA.

C. Superposition of the $GABA_AR$ (in grey) and YGF mutant (in pink) structures highlights key residue differences in the binding pocket after superposing the ECDs. Residues that are different between the two structures are highlighted with rectangles. The Cα atoms of key residues are represented as spheres.

D. Schematic diagram illustrating the changes in distances of the Cα atoms of R81, F175, S145 and T220 in the GlyR and $GABA_AR$ structures.

E. The open probabilities (Po) of the FL and the triple mutant (F115Y+F175Y+F223Y) elicited by 100 mM GABA. Error bars represent SEM and $n \geqslant 6$ cells for all experiments.

Figure S11 Conformational changes between the open, desensitized and closed states of GABA-bound GlyR in SMA. Related to Figure 5.

A. Reference orientation of the GABA-open state. The binding pocket in the ECD, the ECD-TMD interface and TMD are indicated by a black solid, a black dashed and a purple solid rectangle.

B-C. Conformational changes in the TMD between the GABA-closed, GABA-open and GABA-desensitized states. The centers of mass (COM) of the four TM helices from one subunit are indicated. The rotation angle of the COM relative to the receptor center is labeled. The GABA-

open, GABA-desensitized and GABA-closed states are colored in gray, violet and green, respectively.

D-I. Superposition of the (-) subunit to visualize the relative movements in the (+) subunit. Hydrogen bonds are shown in dashed lines. The Cα atoms of key residues in the GABA-open and GABA-closed state are highlighted by gray and green spheres, respectively. (**D. G**) Comparison of the binding pocket (**D**) and ECD-TMD interfaces (**G**) between GABA-open and GABA-desensitized states. (**E. H**) Conformational changes in the binding pockets (**E**) and the ECD-TMD interfaces (**H**) between GABA-closed, GABA-open states. (**F. I**) Schematic diagrams illustrating the changes in distances of the Cα atoms of key residues in the binding pockets (**F**) and ECD-TMD interfaces (**I**) between GABA-open and GABA-closed states.

Figure S12 Conformational changes in the ECD, ECD-TMD and TMD in the partial agonist bound states. Related to Figures 3 and 5.

A-E. Superposition of two adjacent subunits from the closed state in complex with taurine in SMA (taurine-closed) with the resting state of the GlyR (apo-$GlyR_{EM}$) and 5-HT3A receptor (5-$HT_{3A}R$) (PDB code: 6BE1) to show the differences in the binding pocket (black box) and ECD-TMD interfaces (red box). The taurine-closed, apo-$GlyR_{EM}$ and 5-$HT_{3A}R$ are colored in cyan, red and purple, respectively. Taurine is shown in sticks.

F-H. Superposition of the two adjacent subunits of the taurine-closed state with the GABA-closed state to illustrate the changes in the ECD and ECD-TMD interfaces. Cα atoms of key residues are represented as colored circles. The schematic diagram illustrates the changes in distances (angstrom) of key residues for the taurine-closed and GABA-closed states. The taurine-closed and GABA-closed are cyan and green, respectively.

I-J. Conformational changes in the TMD between the taurine-closed, taurine-open and taurine-desensitized states. The centers of mass (COM) of the four TM helices from one subunit are indicated. The rotation angle of the COM relative to the receptor center is labeled. The taurine-closed, taurine-open and taurine-desensitized states are in cyan, yellow and salmon, respectively.

Figure S13 Conformational changes between resting and closed partial agonist-bound states. Related to Figure 5.

607 **A.** Two subunits derived from the GABA-bound SMA closed state, highlighting the
608 neurotransmitter binding site (solid box) and the ECD-TMD interface (dashed box). Superposition
609 of two adjacent subunits from the closed state of GlyR in complex with GABA in SMA (GABA-
610 closed) with the resting state of GlyR (apo-$GlyR_{EM}$) (**B. D**) and 5-HT_{3A} receptor (5-HT_{3A}R) (PDB
611 code: 6BE1) (**C. E**) to show the differences in the binding pocket and ECD-TMD interfaces. The
612 GABA-closed, apo-$GlyR_{EM}$ and 5-HT_{3A}R are colored in green, red and purple, respectively.

613

STAR★METHODS

RESOURCE AVAILABLITY

Lead Contact

Further information and requests for materials should be directed to the Lead Contact, Eric Gouaux (gouauxe@ohsu.edu).

Materials Availability

We are glad to share the associated plasmids in this work upon completion of a Material/Data Transfer Agreement for non-commercial usage. This study did not generate new unique reagents.

Data and Code Availability

The data that support the findings of this study are available from the corresponding author upon request. The following Protein Data Bank (PDB) and Electron Microscopy Data Bank (EMDB) accession codes are provided: 6PM6 and 20389 (GlyR-gly-open-SMA), 6PM5 and 20388 (GlyR-gly-desensitized-SMA), 6PM4 and 20386 (GlyR-gly-expanded-open-SMA), 6PM3 and 20385 (GlyR-taurine-closed-SMA), 6PM2 and 20384 (GlyR-taurine-open-SMA), 6PM1 and 20383 (GlyR-taurine-desensitized-SMA) 6PM0 and 20382 (GlyR-taurine-expanded-open-SMA), 6PLZ and 20381 (GlyR-GABA-closed-SMA), 6PLY and EMD-20380 (GlyR-GABA-open-SMA), 6PLX and 20379 (GlyR-GABA-desensitized-SMA), 6PLW and 20378 (GlyR-GABA-expanded-open-SMA), 6PLO and 20370 (YGF-GABA-open-SMA), 6PLP and 20371(YGF-GABA-desensitized-SMA), 6PLQ and 20372 (YGF-GABA-expanded-open-SMA), 6PXD and 20518 (apo-$GlyR_{EM}$), 6PLR and 20373 (GlyR-gly-desensitized-nanodisc), 6PLT and 20375 (GlyR-taurine-desensitized-nanodisc), 6PLS and 20374 (GlyR-GABA-closed-nanodisc), 6PLV and 20377 (GlyR-GABA-desensitized-nanodisc), and 6PLU and 20376 (GlyR-GABA-closed-nanodisc).

EXPERIMENTAL MODEL AND SUBJECT DETAILS

Cell lines-SF9 cells (CRL-1573) were cultured in sf9-900 III SFM (ThermolFisher Scientific) at 27 °C. These cells were used for expression of Baculovirus and receptor. They are female in origin. Human embryonic kidney 293A cells (HEK293A; ATCC, Teddington, UK, Cat. No. PTA-4488, RRID:CVCL0045) were used for transient expression of GlyRs. HEK293A cells were cultured in 25 cm^2 vented culture flasks containing 5 ml of Dulbecco's modified Eagle's medium (DMEM; Gibco Thermo Fisher, Loughborough, UK, Cat. No. 41966-029) supplemented with 10% (v/v) heat-inactivated fetal bovine serum (Gibco Cat. No. 10500-064), 2 mM glutamine (Invitrogen) and 100 units/ml penicillin/ 100 microg/ml streptomycin (Gibco Cat. No. 15140-122). For expression, cells were plated on poly-L-lysine–coated glass coverslips (Sigma-Aldrich and VWR,

647 respectively) in 35-mm culture dishes (Scientific Laboratory Supplies) containing 2 ml of DMEM,
648 and then transfected via the calcium phosphate- precipitation method with pcDNA3.1 plasmids
649 coding for GlyRs. Cells were washed 5-16 hrs later and electrophysiological experiments were
650 performed 1-2 days after transfection.

651 **METHOD DETAILS**

652 **Protein purification**

653 The cDNA encoding the full-length zebrafish α1 glycine receptor (GlyR, NP_571477), with
654 the following modifications, was cloned into the pFastBac1 vector for baculovirus expression in
655 Sf9 insect cells (Du et al., 2015). We used two GlyR constructs for the studies described here.
656 For all of the experiments, other than the apo state cryo-EM studies, we used the full length GlyR
657 modified only by the addition of a thrombin site (Leu-Val-Pro-Arg-Gly-Ser) and an octa-histidine
658 tag at the carboxy terminus. We refer to this construct as the full length (FL) GlyR. For structure
659 determination of the apo state, we employed the previously described $GlyR_{EM}$ construct in which
660 the M3-M4 loop was replaced by an Ala-Gly-Thr tripeptide (Du et al., 2015). The YGF mutant,
661 where residues Phe175 and Tyr177 were swapped, was generated from FL using site-directed
662 mutagenesis.

663 Following transduction of insect cells with baculovirus and cell culture at 27°C for 72 hours,
664 cells of the FL receptor and apo-$GlyR_{EM}$ were collected and resuspended in a buffer composed
665 of 20 mM Tris pH 8.0 and 150 mM NaCl (TBS) in the presence of 0.8 μM aprotinin, 2 μg/ml
666 leupeptin, 2 mM pepstain A and 1 mM phenylmethylsulfonyl fluoride and disrupted by sonication.
667 Membranes were isolated by centrifugation for 1 h at 200,000 g. For the FL receptor, membrane
668 fraction was collected and solubilized in 20 mM n-dodecyl-β-D-maltopyranoside (C12M) and 2.5
669 mM cholesteryl hemisuccinate Tris salt (CHS) for 2 hours with slow stirring at 4°C. After
670 ultracentrifugation to clarify the solution, the supernatant was collected and incubated with Talon
671 resin for 1 hour and washed with TBS buffer supplemented with 1 mM C12M, 0.25 mM CHS and
672 35 mM imidazole. The receptor was eluted from the affinity resin using a buffer containing 250
673 mM imidazole. Fractions were pooled togethe3r and applied to a size-exclusion chromatography
674 (SEC) Superose 6 10/300 GL column for further purification using a TBS buffer supplemented
675 with 1 mM C12M and 0.25 mM CHS. The peak fractions were collected and concentrated to ~16
676 μM receptor concentration for reconstitution into lipid nanodiscs studies.

677 For the apo-$GlyR_{EM}$, to remove unbound and bound glycine to enable determination of the
678 apo-$GlyR_{EM}$ structure, all the buffers were prepared using HPLC water (Sigma) and extensive

dialysis was carried out as follows. The pelleted membrane with a volume of 30 ml was homogenized and incubated with 100 nM strychnine. The strychnine saturated membranes were transferred to an 8-10 kDa molecular weight cut off cellulose ester dialysis tubing (Spectra/PorBiotech) and dialyzed in 200-fold volume of glycine-free buffer containing 150 mM NaCl, 20 mM Tris 8.0 (TBS buffer in HPLC water) in the presence of 1 mM PMSF, 0.8 µM aprotinin, 2 µg/ml leupeptin, and 2 mM pepstatin A. Buffer exchange was carried out twice a day over the course of five days at 4°C, resulting in 10 changes and an estimated dilution of the original buffer by 10^{20} fold. The purification strategy was the same as that for the FL receptor. The peak fractions after SEC were used for cryo-EM studies.

Nanodisc reconstitution

To incorporate the receptor in lipid nanodiscs (Denisov and Sligar, 2016), brain total lipid extract (BTL, Avanti) dissolved in chloroform was dried down using a rotary evaporator and resuspended in a TBS buffer supplemented with 20 mM C12M and 2.5 mM CHS to a final lipid concentration of 10 mM. Because we estimate that the diameter of the GlyR transmembrane domain is ~80 Å, we used the MSP1E3D1 scaffold protein which, in turn, yields nanodiscs with an outer diameter of ~12 nm. MSP1E3D1 was purified through a metal chelate affinity column (Ni-NTA) and extensive dialysis against TBS buffer (Alvarez et al., 2010). FL receptor was mixed with MSP1E3D1 and BTL in a final ratio of 1: 7.5: 200 (molar ratios) and incubated for 40 min by gentle agitation at 4°C. Detergent was removed by adding Bio-Beads (SM2, Bio-Rad) to a final concentration of 150 mg/ml. After incubation for 2 hours, the Bio-Beads were replaced with fresh beads. The mixture was incubated overnight at 4°C. After separation from Bio-beads, the protein was loaded onto a Superose 6 10/300 GL column equilibrated with TBS buffer. Peak fractions corresponding to reconstituted GlyR were collected for cryo-EM analysis and scintillation-proximity assay (SPA) (Nelson, 1987).

Protein purification via styrene maleic acid (SMA) copolymer solubilization

The SMA copolymer XIRAN 30010 (~2.3:1 molar ratio of stryrene: maleic acid) was purchased from Polyscope as an aqueous solution of 20% (w/v) SMA. The purification procedures in the context of the SMA copolymer are similar to those previously described except for the following differences. Following collection of the membrane fraction by centrifugation, the membranes were resuspended in TBS buffer and XIRAN 30010 was added to a final concentration of 0.5% with slow stirring at 4°C for 1 h. After ultracentrifugation for 1 hr at 200,000 g, the supernatant was collected and incubated with NTA metal ion affinity resin for 5-6 hours.

The remaining purification steps were carried out as described above with the caveat that no additional SMA or detergents were added throughout the remaining purification steps. Following SEC chromatography, the FL/YGF mutant-SMA complex was concentrated to 2 mg/ml for cryo-EM analysis.

Determination of glycine contamination

Potential glycine contamination in 50 mg/ml stocks of taurine or GABA was analyzed using liquid chromatography tandem mass spectrometry (LC-MS/MS) with electrospray ionization in positive mode. MRM (multiple reaction monitoring) transitions monitored specific product ion fragment from glycine. The reported major fragments were 75.9/48 and 75.9/30.2. Standards spiked with 0.1 µg/ml to 50 µg/ml glycine in the presence of a constant concentration of 50 mg/ml of GABA or taurine were prepared as a control to test assay sensitivity. The glycine contents in the 50 mg/ml stocks of taurine or GABA were below the lower limit of detection, 0.1 µg/ml. These experiments allowed us to estimate that the extent of glycine contamination was less than 1.33 µM of glycine in 0.4 M of taurine or 0.49 M of GABA.

Ligand binding assay

Competition ligand binding experiments were carried out using the SPA (Nelson, 1987) and a solution containing 40 nM FL receptor or YGF mutant reconstituted into the SMA, 1 mg/ml Cu-Ysi beads, 0.1% bovine serum albumin, TBS buffer and 100 nM ^{3}H-labelled strychnine (1:9 ^{3}H:^{1}H). The stocks of cold competitors - glycine, taurine and GABA – were prepared in TBS at final concentrations of 0.1M, 0.5M and 1M respectively, followed by serial dilution. To estimate the extent of non-specific binding, 250 mM imidazole was used for background subtraction. The binding reactions reached equilibration after an overnight (<12 hr) incubation and the scintillation counts from the beads were read on a Micro Beta TriLux 1450 LSC & Luminescence Counter (Perkin Elmer). Ki values were determined with the Cheng–Prusoff equation in GraphPad Prism.

Cryo-EM sample preparation and data acquisition

To prepare the GlyR complexes with different agonists, the FL receptor complexes in nanodisc or SMA were mixed with 10 mM glycine, 20 mM taurine or 40 mM GABA immediately before the samples were placed onto the grids. Apo-GlyR_{EM} sample was placed onto the grid directly. Preparation of the YGF mutant complexes with 40 mM GABA followed the same procedures as with the FL type receptor. We estimate that the time elapsed between mixing of receptor with agonist and plunge freezing of the grids was around 10 s. In addition, the extent of

glycine contamination in the taurine and GABA chemicals was estimated as less than 1.33 µM in 0.4 M of taurine or 0.49 M of GABA, as described above. To minimize preferred orientation, the nanodisc-reconstituted receptor solutions were supplemented with 60 µM perfluoro octyl maltoside (FOM) prior to grid preparation. A 2.5 µL sample of receptor was applied to glow-discharged Quantifoil R1.2/1.3 or 2/2 200 mesh gold holey carbon grids which were then blotted for 2.5 s under 100% humidity at 12 °C. The grids were then flash-frozen in liquid ethane, maintained at melting temperature, using a FEI Mark IV cryo-plunge instrument.

Cryo-EM datasets for the receptor-nanodisc complexes were collected on a Talos Arctica microscope (FEI) operated at 200 kV. Images were acquired on a K2 Summit direct-detector (Gatan) using super-resolution mode at a magnification of x45,000, corresponding to a pixel size of 0.455 Å. The defocus range was set from -0.8 µm to -2.2 µm. Each micrograph was recorded over 100 frames at a dose rate of ~5.49 e^-/pixel/s and a total exposure time of 10 s, resulting in a total dose rate of 61 $e^-/Å^2$.

For the FL receptor complexes in SMA, all the datasets were collected on a 300 kV FEI Titan Krios microscope equipped with an energy filter (Gatan Image Filter) set to 20 eV. Images were acquired on a K2 Summit direct-detector positioned after the energy filter using super-resolution mode at 165,000 magnification and a pixel size of 0.412 Å. Images were collected using 'multishot' methods driven by SerialEM (Mastronarde, 2005) with seven shots per hole, utilizing 2/2 200 mesh grids and a defocus ranging from -1.0 µm to -2.0 µm. Each micrograph was recorded over 40 frames with a total dose of 42 $e^-/Å^2$. For the YGF mutant in complex with GABA, the dataset was collected on the same Titan Krios microscope as the FL, but images were acquired on a K3 BioQuantum direct-detector using super-resolution mode at 135,000 magnification with a pixel size of 0.65 Å. Each micrograph was recorded over 60 frames at a dose rate of ~18.76 e^-/pixel/s and a total exposure time of 1.5 s, resulting in total dose rate of 62 $e^-/Å^2$.

The data for apo-$GlyR_{EM}$ was collected on a 300 kV FEI Titan Krios at the cryo-EM facility at HHMI's Janelia Research Campus. This microscope is equipped with a CETCOR Image Corrector for spherical aberration correction and an energy filter. A 20eV energy slit centered on the zero-loss peak, and a C_s of 0.01 mm were used during data collection. All micrographs were recorded on a Gatan K2 Summit direct electron detector operated in super-resolution counting mode with a pixel size of 1.04 Å. The dose-fractionated images were recorded using the automated acquisition program SerialEM (Mastronarde, 2005). Each micrograph was recorded over 30 frames with a total exposure time of 6 s, resulting in a total dose rate of 54 $e^-/Å^2$.

774 **Image processing**

775 Super-resolution image stacks were 2×2 binned in the Fourier space and motion corrected
776 by Motion Cor2 (Zheng et al., 2016). The contrast transfer function (CTF) parameters were
777 estimated by Gctf (Zhang, 2016) and particles were picked by DoG-picker (Voss et al., 2009) for
778 all the datasets except where indicated.

779 We first analyzed the taurine-bound GlyR-nanodisc complex data, culling through the total
780 micrographs and retaining 1,264 micrographs that had Thon rings extending to at least 4 Å.
781 Approximately 669,253 particles were picked from these micrographs and subjected to 2D
782 classification in RELION 2.1 (Scheres, 2012). After several rounds of classification, 2D classes
783 with clearly defined features of the glycine receptor contained 244,309 particles. This particle
784 stack was then employed for subsequent analysis. An initial model generated from cryoSPARC
785 (Punjani et al., 2017) was then used for 3D classification and refinement. A soft mask with
786 extending binary map of 4 pixels and a soft-edge of 6 pixels and C5 symmetry were applied during
787 all the following steps of classification and refinement. Two of the 3D classes (class 1 and class
788 3) showed reasonable secondary structure features and were subjected to 3D refinement, yielding
789 two different maps belonging to what we define as the desensitized and closed states,
790 respectively. To reduce heterogeneity among these two classes and improve the density in the
791 transmembrane regions, class 1 and class 3 were re-classified into three classes. For class 1,
792 this resulted in an additional class 1a (45,300 particles) and class 1b (79,557 particles) with the
793 same transmembrane helix orientation and density. We therefore combined these classes and
794 carried out 3D refinement, which yielded a map that we identify as the taurine-bound desensitized
795 state. For class 3, the resulting class 3b contained only 15,292 particles, albeit with a better
796 density in the transmembrane region. This class was selected for the 3D refinement, yielding a
797 map that we identify as the taurine-bound closed state (Figure S6).

798 A similar procedure was used to process data associated with the GABA-bound receptor
799 in nanodiscs. Briefly, 493,873 particles were auto-picked from 1,109 micrographs and were
800 subjected to 2D and then 3D classification. Two different classes containing 39,926 and 38,383
801 particles were selected for 3D reconstruction and 3D auto-refinement respectively, giving rise to
802 one map that we identify as the GABA-bound desensitized state and a second map that we
803 believe represents the GABA-bound receptor in a closed state (Figure S7).

804 The single particle cryo-EM data for the glycine-bound receptor in nanodiscs was
805 processed using similar procedures. To do this, 472,910 particles were auto-picked from 1,231

806 micrographs and subjected to 2D and 3D classification. Notably, the 3D classes shared the same
807 overall shape and transmembrane helix orientation, suggesting the preponderance of one
808 conformational state in this glycine-bound data set. Three classes (80,121 particles) with good
809 secondary structure features were combined and used for 3D auto-refinement, yielding a map
810 that we define as the glycine-bound desensitized state (Figure S5).

811 For the glycine bound receptor in SMA, a total of 5309 micrographs were retained following
812 the same criteria as above. A total of 1,578k particles were picked by DoG-picker. RELION 3.0
813 (Zivanov et al., 2018) was used for 2D classification, 3D auto-refinement and 3D classification.
814 4× binned particles were extracted followed by one round of 2D classification by limiting the
815 resolution to 8 Å. After this round of 2D classification, only the classes with clear receptor features
816 and clean background were selected. 804k 'good' particles were selected and 2× binned particles
817 were re-extracted followed by one round of 3D refinement using a filtered map and an initial model
818 derived from the previous structure determination of GlyR (PDB code: 3jaf). Additional 3D
819 classification was performed using the refined 2× binned particles by applying C1 or C5 symmetry
820 with alignment with the angular sampling interval of 15^{o} for 25 iterations. The 3D classifications
821 with C1 symmetry yielded similar classes as with C5 symmetry, albeit with slightly weaker TM
822 density, thus justifying use of C5 symmetry. The 172k particles belonging to the dominant class
823 6 were selected and unbinned particles were re-extracted and re-centered followed by another
824 round of 3D refinement. To facilitate the further 3D classification, a mask which includes as much
825 as GlyR density while excluding as much as SMA density as possible was designed. Using the
826 refined unbinned particle stack along with the mask, 6 classes were generated during the 3D
827 classification without alignment until convergence, after 170 iterations. Based on the differences
828 of the M2 helices in these classes, 84,978, 155,456 and 39,586 particles belonging to the putative
829 open state (class 6a), the desensitized state (class 6b), and the 'expanded-open' state (class 6c),
830 respectively, were re-extracted for 3D auto-refinement (Figure S5).

831 Similar procedures were performed for the taurine-bound SMA data set. Here, 5,004
832 movies yielded 1,124k particles that were automatically selected using template based particle
833 picking in RELION 3.0 (Zivanov et al., 2018). 4× binned particles were extracted followed by one
834 round of 2D classification. 543k 'good' particles were retained and unbinned particles were
835 extracted. After 3D classification, four different classes containing 17,873, 17,271, 122,322 and
836 74,365 particles were isolated and were used in 3D auto-refinement, giving rise to the density
837 maps of the taurine-bound closed, taurine-bound desensitized, taurine-bound open and taurine-
838 bound expanded-open states, respectively (Figure S6). For the GABA-bound complex in SMA, a

total of 2,062k particles were extracted from 5,200 micrographs and were subjected to 2D and 3D classification, and then the classes without obvious receptor features were dumped. Four different classes containing 121,470, 150,199, 20,845 and 31,667 particles were selected for 3D reconstruction and 3D auto-refinement respectively, giving rise to four maps that we identify as expanded-open, open, desensitized and closed states, respectively (Figure S7). For the GABA-bound YGF mutant complex in SMA, a total of 1,800k particles extracted from 9,300 micrographs were subjected to 2D and 3D classification. The resulted 407k particles produced two classes containing 32,386, 27,496 and 42,097 particles that we identified as open, desensitized and expanded-open states, respectively (Figure S8).

To further explore the particle fractions in all of the SMA data sets of the FL GlyR complexes, we also used cisTEM (Grant et al., 2018; Zhang et al., 2019) to perform the 3D classification following the procedure and using the parameters as described below. We first created the particle stacks after 2D classification by RELION 3.0 (Scheres, 2016; Zivanov et al., 2018) and then imported these particle stacks into cisTEM. A subsequent auto 3D refinement was performed in cisTEM. Based on the cisTEM refined stacks, we then created a new stack by specifying 15 3D classes. A focused refinement without alignment targeting the TMD was performed with the specified center of 131,131,145 (in Å) located at the TMD, a radius of 36 Å and high resolution limit of 5 Å for 30 iterations. Shown in Table S7 are the results of 3D classification using RELION 3.0 and cisTEM.

For the apo-$GlyR_{EM}$ image processing, approximately 1,000 particles were manually picked for an initial reference-free 2D classification. Seven to eight representative 2D class averages were selected as templates for automated particle picking using RELION 2.1 (Scheres, 2012) or GAUTOMATCH (www.mrc-lmb.cam.ac.uk/kzhang/Gautomatch/). The auto-picked particles were visually checked and false positives were removed, giving rise to 204,323 total particles. The particles were further cleaned-up by 2D classification using RELION 2.1 (Scheres, 2012). The reconstruction of the published gly-EM complex (EMD-6345) was low-pass filtered to 60 Å and used as an initial model. No symmetry was applied during 3D classification in RELION 2.1 (Scheres, 2012). Classes with characteristic features of pLGICs were then selected. Particles belonging to the chosen classes, with a number of 115,864, were used for 3D auto-refinement (Figure S8).

To improve the density in the transmembrane region, all the refined maps from RELION 2.1/3.0 (Scheres, 2012; Zivanov et al., 2018) were further refined using auto refinement in cisTEM (Grant et al., 2018), yielding well-defined maps. The final reconstructions for the receptor in the

nanodiscs were subjected to post-processing in RELION 2.1 (Scheres, 2012), and for the reconstructions of the receptor in SMA the maps were sharpened by Localscale (Jakobi et al., 2017). Local resolution was determined by RELION 3.0 (Zivanov et al., 2018). The reported resolutions in the Table S1 and Table S2 were estimated by gold standard FSC 0.143 criteria (Chen et al., 2013).

Model building

The model building commenced with rigid body fitting of an initial model derived from the prior GlyR structures to each density map followed by real space refinement in Coot (Emsley and Cowtan, 2004) and by using Phenix (Afonine et al., 2018). To build all of the desensitized protein structures, the taurine-bound desensitized state structure in nanodisc (taurine_desensitized_nanodisc) was first built and then was used as the initial structure for the other desensitized state complexes. We began by fitting the glycine/ivermectin-bound protein structure (PDB code: 3jaf), excluding the ligands, into the taurine-bound desensitized state map using UCSF Chimera (Pettersen et al., 2004). The resulting structure was manually adjusted in Coot, guided by well resolved side chain densities. Amino acid residues missing from the previously determined glycine/ivermectin protein structure were added, including H327 at the end of the M3 helix and E390, M391 and R392at the beginning of the M4 helix. Prominent tube-shaped electron density surrounding the receptor transmembrane domain (TMD) likely arises from ordered lipid molecules and thus alkane chains with appropriate lengths were placed in the density features. The structure was further refined using Phenix in the context of restraints for stereochemistry of the alkane chains and carbohydrate groups. After Phenix refinement, the map to model cross correlation (cc) value between the final model and the map was 0.83. To build the other desensitized state structures, the above determined structure taurine_desensitized_nanodisc was fitted to the density maps using UCSF chimera. After rigid-body fitting of the taurine_desensitized_nanodisc model, taurine was replaced with the appropriate ligands, alkane chains were either replaced with appropriate lengths in these nanodisc structures or removed in the SMA structures, and the models were then real-space refined in Coot and Phenix. Specifically, two amino acids - V388 and E399 - were added at the beginning of the M4 helix in these protein structures of the desensitized state in SMA.

The procedures to build the open/expanded-open state protein structures were similar to the model building of the desensitized protein structures. The glycine-bound open state protein structure in SMA (glycine_open_SMA) was achieved by fitting the glycine-bound desensitized protein structure in SMA (glycine_desensitized_SMA) to its corresponding map using UCSF

Chimera. Coot was then used to manually adjust the glycine_desensitized_SMA structure, mainly focusing on the TMD, followed by Phenix refinement, yielding a map to model cc of 0.80. To build the taurine-bound and GABA-bound open/expanded-open state protein structures derived from the receptor-SMA complex, the glycine_open_SMA structure was simply fit to the corresponding maps using UCSF Chimera, following by fitting of the appropriate ligands to the density in the neurotransmitter binding pocket. Phenix real space refinement was next performed to refine the protein structures within their corresponding density maps.

To build the GABA-bound YGF mutant open, desensitized and expanded-open states, the two amino acids 175F and 177Y were firstly mutated into 175Y and 177F by Coot, respectively, within their corresponding FL GABA-bound structures. After Phenix refinement, the resulted map to model cc values were 0.80, 0.79 and 0.72 for YGF mutant open, desensitized and expanded-open states, respectively.

For model building of the taurine-bound closed state in nanodisc (taurine_closed_nanodisc), we found that the previously determined strychnine-bound structure (PDB code: 3jad) fit the map well and thus it was used as an initial model. The structure was fit to the taurine-bound closed state map using UCSF Chimera. Chain A of the superimposed model was further optimized by real space refinement using Coot, including fitting of a taurine molecule to the density in the neurotransmitter binding pocket, adding Q326 and H327 at the end of the M3 and E390, M391 and R392 at the beginning of M4 helices, manually building the M2-M3 loop and adding lipid-derived alkane chains surrounding TMD. The model generated in Coot was further refined against the density map by Phenix. The cc between the taurine_closed_nanodisc and its corresponding map was 0.81. To build the other state protein structures either in nanodisc or SMA, the Phenix refined taurine_closed_nanodisc coordinates were used as the initial structure. Coot was used to change the ligands and remove the alkane chains in SMA structures or replace with appropriate chain lengths in nanodisc structures based on the density features, followed by Phenix refinement. All of the final models have good stereochemistry as evaluated by molprobity (Chen et al., 2010) (Tables S1-S4). All the figures were prepared by Pymol (Schrödinger, LLC) and UCSF chimera (Pettersen et al., 2004). Pore radii were calculated using program HOLE (Smart et al., 1996).

Patch-clamp and single-channel recording

Heterologous expression in human embryonic kidney cells. Full-length zebrafish α1 GlyR was subcloned into the pcDNA3.1 for expression in the human embryonic kidney 293A cells

(HEK293A). Point mutations were made using site-directed mutagenesis. HEK293A cells were transiently transfected using the calcium phosphate-DNA precipitation method. The DNA mix consisted of pcDNA3.1 plasmids with inserts coding for the enhanced Green Fluorescence Protein (eGFP; GenBank accession number U55763), and GlyR (FL or mutant). Plasmid without an open reading frame ("empty") was added to the transfection mix to optimize the expression level (Groot-Kormelink et al., 2002). The final mixture of cDNA contained 2% α1, 18% eEGFP and 80% empty pcDNA3.1 plasmid. Cells were washed 5-16 hrs later and electrophysiological experiments were performed 1-2 days after transfection.

Patch-clamp recordings and analysis. Macroscopic and single-channel currents were recorded from transfected HEK293A cells in the whole-cell, outside-out and cell-attached patch-clamp configurations at 20ºC. Patch electrodes were pulled from thick-walled borosilicate glass capillary tubes (GC150F-7.5; Harvard Apparatus) on a Flaming/Brown puller (Model-P97, Sutter Instruments) and were fire-polished to give a final resistance of 3-5 MΩ for whole-cell recordings and 5-15 MΩ for cell-attached or outside-out recordings (when filled with the appropriate internal solution).

Cells were bathed in an extracellular solution consisting of (in mM): 20 Na D-gluconate, 112.7 NaCl, 2 KCl, 2 CaCl2, 1.2 MgCl2, 10 HEPES (4-(2-hydroxyethyl)-1-piperazineethanesulfonic acid), 40 glucose (all Sigma) and 10 tetraethylammonium chloride (TEACl) (Alfa Aesar); the pH adjusted to 7.4 with NaOH. For the cell-attached recordings, pipettes were filled with extracellular solution containing the required concentration of agonist. To record macroscopic currents, the pipette was filled with a 30 mM chloride intracellular solution, containing (in mM): 101.1 K gluconate, 1 ethylene glycol tetraacetic acid (EGTA), 1 CaCl2, 1 MgCl2, 10 HEPES, 2 MgATP, 40 sucrose, 6 KCl (all Sigma) and 20 TEACl, the pH adjusted to 7.4 with NaOH. All solutions were prepared in bi-distilled water or, for cell-attached single channel recordings, in high-performance liquid chromatography grade (HPLC) water (VWR Chemicals), and filtered through a 0.2 µm cellulose nitrate membrane filter (Whatman) before use. Glycine, taurine or GABA-containing solutions were prepared by diluting a 1 M glycine, 1 M taurine or 1 M GABA stock in extracellular solution.

Taurine and GABA were purified by 2x recrystallization from aqueous ethanol and subsequently tested for glycine contamination by an HPLC assay: samples were resuspended in 10 µl 50% EtOH, reacted for 30 min with 90% EtOH:triethylamine:phenylisothiocyanate (7:2:1), evaporated to dryness at room temperature and redissolved in 100 µl 5% acetonitrile in 0.1 M ammonium acetate. A 150x4.6 mm Hypersil C18 column was used and detection was monitored

970 at 254 nm. The purified taurine and GABA contained no detectable glycine, which in this assay
971 is less than 1 part in 10,000.
972 **Whole-cell recording**. Whole-cell currents were recorded from isolated transfected cells
973 held at a holding potential of −40 mV (corrected for the junction potential of 11 mV) with an
974 Axopatch 200B (Molecular Devices) and filtered at 5 kHz by the amplifier's low pass 4-pole Bessel
975 filter. Recordings were digitized with a Digidata 1440A (Molecular Devices) at a sampling
976 frequency of 20 kHz and acquired to PC using Clampex 10.2 software (Molecular Devices) for
977 offline analysis.
978 Agonist solutions were applied to the cells for approximately 1-2 s by a U-tube application
979 system (Krishtal and Pidoplichko, 1980), with a 10-90% exchange time <1 ms (as tested by
980 application of 50% diluted extracellular solution to the open tip pipette). The saturating agonist
981 concentration was applied every third or fourth application to check response stability throughout
982 the recording. Only cells where the test response rundown was less than 30% during the
983 experiment were accepted for further analysis. No correction for rundown was applied. Different
984 agonist concentrations were applied in random order to obtain concentration-response curves.
985 The peak current amplitudes for each glycine application were measured using Clampfit 10.2
986 software (Molecular Devices). The concentration-response data for each cell were then fitted with
987 the Hill equation using the CVFIT programme (DCPROGS; https://github.com/DCPROGS/CVFIT)
988 to estimate EC50 (agonist concentration required to elicit 50% maximal response), nH (Hill-slope)
989 and Imax (maximum peak current).
990 **Fast agonist application**. Macroscopic currents evoked in outside-out patches by fast
991 agonist application pulses were recorded at a pipette holding potential of −100 mV (−111 mV
992 when corrected for a junction potential of 11 mV). The internal solution was the same as the one
993 for whole cell recordings and contained 30 mM chloride. Agonist, dissolved in extracellular
994 solution, was applied to outside-out patches with a theta tube (Hilgenberg GmbH) cut to a final
995 diameter of $\approx$ 150 μm at the tip. The tube was driven by a piezo stepper PZ-150M (Burleigh
996 Instruments Inc). The exchange time was measured by the application of diluted bath solution
997 (e.g., 30:70 bath solution: water) before the experiment (to optimize the electrode position) and
998 after the rupture of the patch. The rise and decay times for these open-tip currents were measured
999 using Clampfit 10.2 as the times from 20 to 80% of the peak response. Patches in which the open
1000 tip response had a 20–80% exchange time slower than 200 μs were rejected from further analysis.
1001 In order to study the kinetics of macroscopic currents, 10–20 responses were recorded in
1002 response to pulses of agonist applied at intervals of at least 10 s and averaged. Only experiments
1003 in which the rundown between the first and last three responses was < 30% were included in the

analysis. The time course of the macroscopic currents was characterized by fitting the rise time between 20 and 100% and the decay time from 80 to 20% of the peak response with one or more exponentials.

Single-channel recording. Low-noise single-channel currents were recorded in the cell-attached configuration at a pipette holding potential of +100 mV with an Axopatch 200B and filtered at 10 kHz using the amplifier's low pass 4-pole Bessel filter. The data was digitized with a Digidata 1322A (Molecular Devices) at a sampling frequency of 100 kHz and acquired to PC using Clampex 10.2 for offline analysis.

Single channel current amplitude and cluster P_o measurements. In order to compare single-channel current amplitudes and cluster open probability, single-channel recordings were filtered offline using the Clampfit 10.2 low-pass Gaussian filter with a final cut-off of 5 kHz and resampled at 50 kHz. At high agonist concentration, channel openings occurred in clusters delimited by long closed intervals, likely to be desensitized. These clusters are likely to originate from the activity of a single ion channel molecule and were used for $\mathbf{P_o}$ measurements. Clusters longer than 100 ms with more than 10 openings were selected for analysis. The gap between clusters was at least 100 ms or 300 ms (for GABA measurements). Channel activity in the selected clusters was idealized using the half-amplitude threshold method implemented in Clampfit 10.2 and open probability was calculated as the ratio of cluster open time over total cluster length. The amplitude of single channel currents was measured in Clampfit 10.2 as the average of all detected opening amplitudes inside a cluster. Electrophysiological data are reported as means ± SEM.

QUANTIFICATION AND STATISTICAL ANALYSIS

For the competitive inhibition radioligand-binding experiment, specific counts with standard deviations were counted by subtracting background nonspecific counts from triplicate experiments. Ki values were obtained from the IC50 values using the Cheng-Prusoff equation by fitting data to a standard single site competition equation. All the values are included in the analysis.

References

Afonine, P.V., Poon, B.K., Read, R.J., Sobolev, O.V., Terwilliger, T.C., Urzhumtsev, A., and Adams, P.D. (2018). Real-space refinement in PHENIX for cryo-EM and crystallography. Acta Crystallogr D Struct Biol *74*, 531-544.

Althoff, T., Hibbs, R.E., Banerjee, S., and Gouaux, E. (2014). X-ray structures of GluCl in apo states reveal a gating mechanism of Cys-loop receptors. Nature *512*, 333-337.

Alvarez, F.J., Orelle, C., and Davidson, A.L. (2010). Functional reconstitution of an ABC transporter in nanodiscs for use in electron paramagnetic resonance spectroscopy. J Am Chem Soc *132*, 9513-9515.

Auerbach, A. (2005). Gating of acetylcholine receptor channels: brownian motion across a broad transition state. Proc Natl Acad Sci U S A *102*, 1408-1412.

Auerbach, A., and Akk, G. (1998). Desensitization of mouse nicotinic acetylcholine receptor channels. A two-gate mechanism. J Gen Physiol *112*, 181-197.

Autzen, H.E., Julius, D., and Cheng, Y. (2019). Membrane mimetic systems in CryoEM: keeping membrane proteins in their native environment. Curr Opin Struct Biol *58*, 259-268.

Baenziger, J.E., Henault, C.M., Therien, J.P., and Sun, J. (2015). Nicotinic acetylcholine receptor-lipid interactions: Mechanistic insight and biological function. Biochim Biophys Acta *1848*, 1806-1817.

Basak, S., Gicheru, Y., Samanta, A., Molugu, S.K., Huang, W., Fuente, M., Hughes, T., Taylor, D.J., Nieman, M.T., Moiseenkova-Bell, V.*, et al.* (2018). Cryo-EM structure of 5-HT3A receptor in its resting conformation. Nat Commun *9*, 514.

Bormann, J., Hamill, O.P., and Sakmann, B. (1987). Mechanism of anion permeation through channels gated by glycine and gamma-aminobutyric acid in mouse cultured spinal neurones. J Physiol *385*, 243-286.

Breitinger, H.G., Lanig, H., Vohwinkel, C., Grewer, C., Breitinger, U., Clark, T., and Becker, C.M. (2004). Molecular dynamics simulation links conformation of a pore-flanking region to hyperekplexia-related dysfunction of the inhibitory glycine receptor. Chem Biol *11*, 1339-1350.

Burzomato, V., Beato, M., Groot-Kormelink, P.J., Colquhoun, D., and Sivilotti, L.G. (2004). Single-channel behavior of heteromeric alpha1beta glycine receptors: an attempt to detect a conformational change before the channel opens. J Neurosci *24*, 10924-10940.

Celie, P.H., van Rossum-Fikkert, S.E., van Dijk, W.J., Brejc, K., Smit, A.B., and Sixma, T.K. (2004). Nicotine and carbamylcholine binding to nicotinic acetylcholine receptors as studied in AChBP crystal structures. Neuron *41*, 907-914.

Cerdan, A.H., Martin, N.E., and Cecchini, M. (2018). An Ion-Permeable State of the Glycine Receptor Captured by Molecular Dynamics. Structure *26*, 1555-1562 e1554.

Changeux, J.P. (2012). Allostery and the Monod-Wyman-Changeux model after 50 years. Annu Rev Biophys *41*, 103-133.

Changeux, J.P., and Edelstein, S.J. (1998). Allosteric receptors after 30 years. Neuron *21*, 959-980.

Chen, S., McMullan, G., Faruqi, A.R., Murshudov, G.N., Short, J.M., Scheres, S.H., and Henderson, R. (2013). High-resolution noise substitution to measure overfitting and validate

1074 resolution in 3D structure determination by single particle electron cryomicroscopy.
1075 Ultramicroscopy *136*, 24-35.

1076 Chen, V.B., Arendall, W.B., 3rd, Headd, J.J., Keedy, D.A., Immormino, R.M., Kapral, G.J., Murray,
1077 L.W., Richardson, J.S., and Richardson, D.C. (2010). MolProbity: all-atom structure validation for
1078 macromolecular crystallography. Acta Crystallogr D Biol Crystallogr *66*, 12-21.

1079 Colquhoun, D. (1998). Binding, gating, affinity and efficacy: the interpretation of structure-activity
1080 relationships for agonists and of the effects of mutating receptors. Br J Pharmacol *125*, 924-947.

1081 Colquhoun, D., and Sakmann, B. (1985). Fast events in single-channel currents activated by
1082 acetylcholine and its analogues at the frog muscle end-plate. J Physiol *369*, 501-557.

1083 Corradi, J., and Bouzat, C. (2014). Unraveling mechanisms underlying partial agonism in 5-HT3A
1084 receptors. J Neurosci *34*, 16865-16876.

1085 Corradi, J., Gumilar, F., and Bouzat, C. (2009). Single-channel kinetic analysis for activation and
1086 desensitization of homomeric 5-HT(3)A receptors. Biophys J *97*, 1335-1345.

1087 Del Castillo, J., and Katz, B. (1957). Interaction at end-plate receptors betwen different choline
1088 derivatives. Proc Roy Soc B *146*, 369-381.

1089 Denisov, I.G., and Sligar, S.G. (2016). Nanodiscs for structural and functional studies of
1090 membrane proteins. Nat Struct Mol Biol *23*, 481-486.

1091 Dorr, J.M., Scheidelaar, S., Koorengevel, M.C., Dominguez, J.J., Schafer, M., van Walree, C.A.,
1092 and Killian, J.A. (2016). The styrene-maleic acid copolymer: a versatile tool in membrane research.
1093 Eur Biophys J *45*, 3-21.

1094 Du, J., Lu, W., Wu, S., Cheng, Y., and Gouaux, E. (2015). Glycine receptor mechanism elucidated
1095 by electron cryo-microscopy. Nature *526*, 224-229.

1096 Emsley, P., and Cowtan, K. (2004). Coot: model-building tools for molecular graphics. Acta
1097 Crystallogr D Biol Crystallogr *60*, 2126-2132.

1098 Fucile, S., de Saint Jan, D., David-Watine, B., Korn, H., and Bregestovski, P. (1999). Comparison
1099 of glycine and GABA actions on the zebrafish homomeric glycine receptor. J Physiol *517 (Pt 2)*,
1100 369-383.

1101 Gielen, M., Thomas, P., and Smart, T.G. (2015). The desensitization gate of inhibitory Cys-loop
1102 receptors. Nat Commun *6*, 6829.

1103 Gonzalez-Gutierrez, G., Wang, Y., Cymes, G.D., Tajkhorshid, E., and Grosman, C. (2017).
1104 Chasing the open-state structure of pentameric ligand-gated ion channels. J Gen Physiol *149*,
1105 1119-1138.

1106 Grant, T., Rohou, A., and Grigorieff, N. (2018). cisTEM, user-friendly software for single-particle
1107 image processing. Elife *7*.

1108 Groot-Kormelink, P.J., Beato, M., Finotti, C., Harvey, R.J., and Sivilotti, L.G. (2002). Achieving
1109 optimal expression for single channel recording: a plasmid ratio approach to the expression of
1110 alpha 1 glycine receptors in HEK293 cells. J Neurosci Methods *113*, 207-214.

1111 Hansen, S.B., Sulzenbacher, G., Huxford, T., Marchot, P., Taylor, P., and Bourne, Y. (2005).
1112 Structures of Aplysia AChBP complexes with nicotinic agonists and antagonists reveal distinctive
1113 binding interfaces and conformations. EMBO J *24*, 3635-3646.

1114 Heidmann, T., Sobel, A., Popot, J.L., and Changeux, J.P. (1980). Reconstitution of a functional
1115 acetylcholine receptor. Conservation of the conformational and allosteric transitions and recovery
1116 of the permeability response; role of lipids. Eur J Biochem *110*, 35-55.

1117 Hibbs, R.E., and Gouaux, E. (2011). Principles of activation and permeation in an anion-selective
1118 Cys-loop receptor. Nature *474*, 54-60.

1119 Hilf, R.J., and Dutzler, R. (2008). X-ray structure of a prokaryotic pentameric ligand-gated ion
1120 channel. Nature *452*, 375-379.

1121 Hille, B. (2001). Ion channels of excitable membranes, 3rd edn (Sunderland, MA: Sinauer
1122 Associates, Inc.).

1123 Huang, X., Chen, H., Michelsen, K., Schneider, S., and Shaffer, P.L. (2015). Crystal structure of
1124 human glycine receptor-alpha3 bound to antagonist strychnine. Nature *526*, 277-280.

1125 Huang, X., Chen, H., and Shaffer, P.L. (2017a). Crystal Structures of Human GlyRalpha3 Bound
1126 to Ivermectin. Structure *25*, 945-950 e942.

1127 Huang, X., Shaffer, P.L., Ayube, S., Bregman, H., Chen, H., Lehto, S.G., Luther, J.A., Matson,
1128 D.J., McDonough, S.I., Michelsen, K.*, et al.* (2017b). Crystal structures of human glycine receptor
1129 alpha3 bound to a novel class of analgesic potentiators. Nat Struct Mol Biol *24*, 108-113.

1130 Jadey, S., and Auerbach, A. (2012). An integrated catch-and-hold mechanism activates nicotinic
1131 acetylcholine receptors. J Gen Physiol *140*, 17-28.

1132 Jakobi, A.J., Wilmanns, M., and Sachse, C. (2017). Model-based local density sharpening of cryo-
1133 EM maps. Elife *6*.

1134 Jamshad, M., Lin, Y.P., Knowles, T.J., Parslow, R.A., Harris, C., Wheatley, M., Poyner, D.R., Bill,
1135 R.M., Thomas, O.R., Overduin, M.*, et al.* (2011). Surfactant-free purification of membrane proteins
1136 with intact native membrane environment. Biochem Soc Trans *39*, 813-818.

1137 Janzen, D., Schaefer, N., Delto, C., Schindelin, H., and Villmann, C. (2017). The GlyR
1138 Extracellular beta8-beta9 Loop - A Functional Determinant of Agonist Potency. Front Mol
1139 Neurosci *10*, 322.

1140 Katz, B., and Thesleff, S. (1957). A study of the 'desensitization' produced by acetylcholine at the
1141 motor end-plate. J Physiol *138*, 63-80.

1142 Knowles, T.J., Finka, R., Smith, C., Lin, Y.P., Dafforn, T., and Overduin, M. (2009). Membrane
1143 proteins solubilized intact in lipid containing nanoparticles bounded by styrene maleic acid
1144 copolymer. J Am Chem Soc *131*, 7484-7485.

1145 Krishtal, O.A., and Pidoplichko, V.I. (1980). A receptor for protons in the nerve cell membrane.
1146 Neuroscience *5*, 2325-2327.

1147 Kumar, A., Basak, S., Rao, S., Gicheru, Y., Mayer, M.L., Sansom, M.S.P., and Chakrapani, S.
1148 (2020). Mechanisms of activation and desensitization of full-length glycine receptor in lipid
1149 nanodiscs. Nat Commun *11*, 3752.

1150 Lam, S., and Patel, P.N. (2007). Varenicline: a selective alpha4beta2 nicotinic acetylcholine
1151 receptor partial agonist approved for smoking cessation. Cardiol Rev *15*, 154-161.

1152 Lape, R., Colquhoun, D., and Sivilotti, L.G. (2008). On the nature of partial agonism in the nicotinic
1153 receptor superfamily. Nature *454*, 722-727.

1154 Lape, R., Plested, A.J., Moroni, M., Colquhoun, D., and Sivilotti, L.G. (2012). The alpha1K276E
1155 startle disease mutation reveals multiple intermediate states in the gating of glycine receptors. J
1156 Neurosci *32*, 1336-1352.

1157 Laverty, D., Desai, R., Uchanski, T., Masiulis, S., Stec, W.J., Malinauskas, T., Zivanov, J., Pardon,
1158 E., Steyaert, J., Miller, K.W.*, et al.* (2019). Cryo-EM structure of the human alpha1beta3gamma2
1159 GABAA receptor in a lipid bilayer. Nature *565*, 516-520.

1160 Lu, T., Rubio, M.E., and Trussell, L.O. (2008). Glycinergic transmission shaped by the corelease
1161 of GABA in a mammalian auditory synapse. Neuron *57*, 524-535.

1162 Lynch, J.W. (2004). Molecular structure and function of the glycine receptor chloride channel.
1163 Physiol Rev *84*, 1051-1095.

1164 Lynch, J.W., Han, N.L., Haddrill, J., Pierce, K.D., and Schofield, P.R. (2001). The surface
1165 accessibility of the glycine receptor M2-M3 loop is increased in the channel open state. J Neurosci
1166 *21*, 2589-2599.

1167 Masiulis, S., Desai, R., Uchanski, T., Martin, I.S., Laverty, D., Karia, D., Malinauskas, T., Zivanov,
1168 J., Pardon, E., Kotecha, A.*, et al.* (2019). Author Correction: GABAA receptor signalling
1169 mechanisms revealed by structural pharmacology. Nature.

1170 Mastronarde, D.N. (2005). Automated electron microscope tomography using robust prediction
1171 of specimen movements. J Struct Biol *152*, 36-51.

1172 Miyazawa, A., Fujiyoshi, Y., and Unwin, N. (2003). Structure and gating mechanism of the
1173 acetylcholine receptor pore. Nature *423*, 949-955.

1174 Mortensen, M., Kristiansen, U., Ebert, B., Frolund, B., Krogsgaard-Larsen, P., and Smart, T.G.
1175 (2004). Activation of single heteromeric GABA(A) receptor ion channels by full and partial agonists.
1176 J Physiol *557*, 389-413.

1177 Mukhtasimova, N., daCosta, C.J., and Sine, S.M. (2016). Improved resolution of single channel
1178 dwell times reveals mechanisms of binding, priming, and gating in muscle AChR. J Gen Physiol
1179 *148*, 43-63.

1180 Mukhtasimova, N., Lee, W.Y., Wang, H.L., and Sine, S.M. (2009). Detection and trapping of
1181 intermediate states priming nicotinic receptor channel opening. Nature *459*, 451-454.

1182 Mukhtasimova, N., and Sine, S.M. (2018). Full and partial agonists evoke distinct structural
1183 changes in opening the muscle acetylcholine receptor channel. J Gen Physiol *150*, 713-729.

1184 Nelson, N. (1987). A novel method for the detection of receptors and membrane proteins by
1185 scintillation proximity radioassay. Anal Biochem *165*, 287-293.

1186 Pettersen, E.F., Goddard, T.D., Huang, C.C., Couch, G.S., Greenblatt, D.M., Meng, E.C., and
1187 Ferrin, T.E. (2004). UCSF Chimera--a visualization system for exploratory research and analysis.
1188 J Comput Chem *25*, 1605-1612.

1189 Phulera, S., Zhu, H., Yu, J., Claxton, D.P., Yoder, N., Yoshioka, C., and Gouaux, E. (2018). Cryo-
1190 EM structure of the benzodiazepine-sensitive alpha1beta1gamma2S tri-heteromeric GABAA
1191 receptor in complex with GABA. Elife *7*.

1192 Plested, A.J. (2016). Structural mechanisms of activation and desensitization in neurotransmitter-
1193 gated ion channels. Nat Struct Mol Biol *23*, 494-502.

1194 Punjani, A., Rubinstein, J.L., Fleet, D.J., and Brubaker, M.A. (2017). cryoSPARC: algorithms for
1195 rapid unsupervised cryo-EM structure determination. Nat Methods *14*, 290-296.

1196 Ritchie, T.K., Grinkova, Y.V., Bayburt, T.H., Denisov, I.G., Zolnerciks, J.K., Atkins, W.M., and
1197 Sligar, S.G. (2009). Chapter 11 - Reconstitution of membrane proteins in phospholipid bilayer
1198 nanodiscs. Methods Enzymol *464*, 211-231.

1199 Rundstrom, N., Schmieden, V., Betz, H., Bormann, J., and Langosch, D. (1994).
1200 Cyanotriphenylborate: subtype-specific blocker of glycine receptor chloride channels. Proc Natl
1201 Acad Sci U S A *91*, 8950-8954.

Scheres, S.H. (2012). RELION: implementation of a Bayesian approach to cryo-EM structure determination. J Struct Biol *180*, 519-530.

Scheres, S.H. (2016). Processing of Structurally Heterogeneous Cryo-EM Data in RELION. Methods Enzymol *579*, 125-157.

Schmieden, V., Kuhse, J., and Betz, H. (1992). Agonist pharmacology of neonatal and adult glycine receptor alpha subunits: identification of amino acid residues involved in taurine activation. EMBO J *11*, 2025-2032.

Schmieden, V., Kuhse, J., and Betz, H. (1993). Mutation of glycine receptor subunit creates beta-alanine receptor responsive to GABA. Science *262*, 256-258.

Schwartz, R.D., and Yu, X. (1995). Optical imaging of intracellular chloride in living brain slices. J Neurosci Methods *62*, 185-192.

Smart, O.S., Neduvelil, J.G., Wang, X., Wallace, B.A., and Sansom, M.S. (1996). HOLE: a program for the analysis of the pore dimensions of ion channel structural models. J Mol Graph *14*, 354-360, 376.

Stephenson, R.P. (1956). A modification of receptor theory. Brit J Pharmacol *11*, 379-393.

Sunesen, M., de Carvalho, L.P., Dufresne, V., Grailhe, R., Savatier-Duclert, N., Gibor, G., Peretz, A., Attali, B., Changeux, J.P., and Paas, Y. (2006). Mechanism of Cl- selection by a glutamate-gated chloride (GluCl) receptor revealed through mutations in the selectivity filter. J Biol Chem *281*, 14875-14881.

Tripathy, S., Zheng, W., and Auerbach, A. (2019). A single molecular distance predicts agonist binding energy in nicotinic receptors. J Gen Physiol *151*, 452-464.

Voss, N.R., Yoshioka, C.K., Radermacher, M., Potter, C.S., and Carragher, B. (2009). DoG picker and TiltPicker: software tools to facilitate particle selection in single particle electron microscopy. J Struct Biol *166*, 205-213.

Walsh, R.M., Jr., Roh, S.H., Gharpure, A., Morales-Perez, C.L., Teng, J., and Hibbs, R.E. (2018). Structural principles of distinct assemblies of the human alpha4beta2 nicotinic receptor. Nature *557*, 261-265.

Zhang, C., Cantara, W., Jeon, Y., Musier-Forsyth, K., Grigorieff, N., and Lyumkis, D. (2019). Analysis of discrete local variability and structural covariance in macromolecular assemblies using Cryo-EM and focused classification. Ultramicroscopy *203*, 170-180.

Zhang, J., Xue, F., Liu, Y., Yang, H., and Wang, X. (2013). The structural mechanism of the Cys-loop receptor desensitization. Mol Neurobiol *48*, 97-108.

Zhang, K. (2016). Gctf: Real-time CTF determination and correction. J Struct Biol *193*, 1-12.

Zheng, S., Palowcak, E., Armache, J.-P., Cheng, Y., and Agard, D. (2016). Anisotropic correction of beam-induced motion for improved single-particle electron cryo-microscopy. bioRxiv *doi: http://dx.doi.org/10.1101/061960*.

Zivanov, J., Nakane, T., Forsberg, B.O., Kimanius, D., Hagen, W.J., Lindahl, E., and Scheres, S.H. (2018). New tools for automated high-resolution cryo-EM structure determination in RELION-3. Elife *7*.

KEY RESOURCES TABLE

REAGENT or RESOURCE	SOURCE	IDENTIFIER
Chemicals and Recombinant Proteins		
Sf-900^{TM} III SFM (1X)	GIBCO	Cat#12658-027
Glycine	Sigma	Cat#G7126-100G
Taurine	Sigma	Cat#T0625-100G
γ-Aminobutyric Acid	Sigma	Cat#A2129-100G
Strychnine	Sigma	Cat#S0532-25G
[^{3}H]Strychnine	PerkinElmer	Cat#NET773250UC
DDM	Anatrace	Cat#D310 25GM
CHS	Anatrace	Cat#CH210 25GM
SMA copolymer	Polyscope	Cat#XIRAN SL30010 P20
Deposited Data		
GlyR-glycine, desensitized state, nanodisc	This Study	PDB ID: 6PLR, EMDB ID: EMD-20373
GlyR-taurine, desensitized state, nanodisc	This Study	PDB ID: 6PLS, EMDB ID: EMD-20374
GlyR-taurine, closed state, nanodisc	This Study	PDB ID: 6PLT, EMDB ID: EMD-20375
GlyR-GABA, desensitized state, nanodisc	This Study	PDB ID: 6PLU, EMDB ID: EMD-20376
GlyR-GABA, closed state, nanodisc	This Study	PDB ID: 6PLV, EMDB ID: EMD-20377
GlyR-GABA, expanded-open state, SMA	This Study	PDB ID: 6PLW, EMDB ID: EMD-20378
GlyR-GABA, desensitized state, SMA	This Study	PDB ID: 6PLX, EMDB ID: EMD-20379
GlyR-GABA, open state, SMA	This Study	PDB ID: 6PLY, EMDB ID: EMD-20380
GlyR-GABA, closed state, SMA	This Study	PDB ID: 6PLZ, EMDB ID: EMD-20381
GlyR-taurine, expanded-open state, SMA	This Study	PDB ID: 6PM0, EMDB ID: EMD-20382
GlyR-taurine, desensitized state, SMA	This Study	PDB ID: 6PM1, EMDB ID: EMD-20383
GlyR-taurine, open state, SMA	This Study	PDB ID: 6PM2, EMDB ID: EMD-20384
GlyR-taurine, closed state, SMA	This Study	PDB ID: 6PM3, EMDB ID: EMD-20385
GlyR-glycine, expanded-open state, SMA	This Study	PDB ID: 6PM4, EMDB ID: EMD-20386
GlyR-glycine, desensitized state, SMA	This Study	PDB ID: 6PM5, EMDB ID: EMD-20388
YGF mutant-GABA, open state, SMA	This Study	PDB ID: 6PLO, EMDB ID: EMD-20370

YGF mutant-GABA, desensitized state, SMA	This Study	PDB ID: 6PLP, EMDB ID: EMD-20371
YGF mutant-GABA, expanded-open state, SMA	This Study	PDB ID: 6PLQ, EMDB ID: EMD-20372
$GlyR_{EM}$, apo state, micelle	This Study	PDB ID: 6PXD, EMDB ID: EMD-20518
Experimental Models: Cell lines		
HEK293A	ATCC	Cat#PTA-4488
Sf9	ATCC	CRL-1711
Recombinant DNA		
GlyRα1-pFastBac1	This Study	N/A
$GlyR\alpha1_{EM}$-pFastBac1	This Study	N/A
YGF-pFastBac1	This Study	N/A
GlyRα1-pcDNA3.1	This Study	N/A
YGF-pcDNA3.1	This Study	N/A
YYY-pcDNA3.1	This Study	N/A
eGFP-pcDNA3.1	This Study	GeneBank: U55763
Software and Algorithms		
SerialEM	(Mastronarde, 2005)	https://bio3d.colorado.edu/SerialEM/
UCSF MOTIONCOR2	(Zheng et al., 2016)	https://emcore.ucsf.edu/ucsf-software
Gctf	(Zhang, 2016)	https://www2.mrc-lmb.cam.ac.uk/research/locally-developed-software/zhang-software/
DoG-Picker	(Voss et al., 2009)	https://emg.nysbc.org/redmine/projects/software/wiki/DoGpicker
RELION 2.1/3.0	(Scheres, 2012; Zivanov et al., 2018)	https://www3.mrc-lmb.cam.ac.uk/relion/index.php/Main_Page
CryoSparc	(Punjani et al., 2017)	https://cryosparc.com
cisTEM	(Grant et al., 2018)	https://cistem.org
Phenix	(Afonine et al., 2018)	https://www.phenix-online.org
UCSF Chimera	(Pettersen et al., 2004)	https://www.cgl.ucsf.edu/chimera
COOT	(Emsley and Cowtan, 2004)	https://www2.mrc-lmb.cam.ac.uk/personal/pemsley/coot
PyMOL	Schrodinger	https://pymol.org/2
Other		
TALON metal affinity resin	Takara	Cat#635504

R1.2/1.3 300 mesh Au holey carbon grids	Electron Microscopy Sciences	Cat#Q3100AR1.3
R2/2 200 mesh Au holey carbon grids	TedPella	Cat#657-200-AU-100

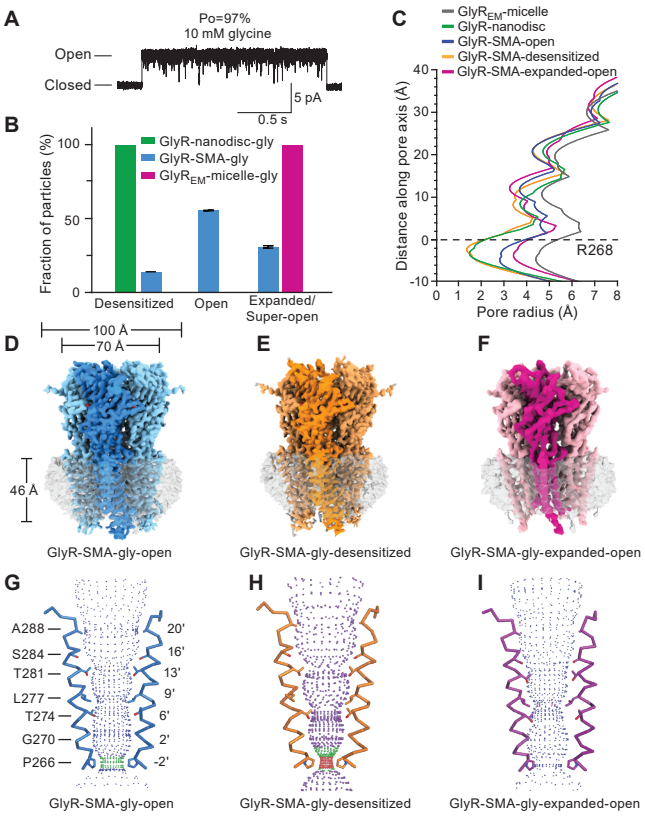

Figure 1

Figure. 2

Click here to access/download;Figure;Figure2.pdf

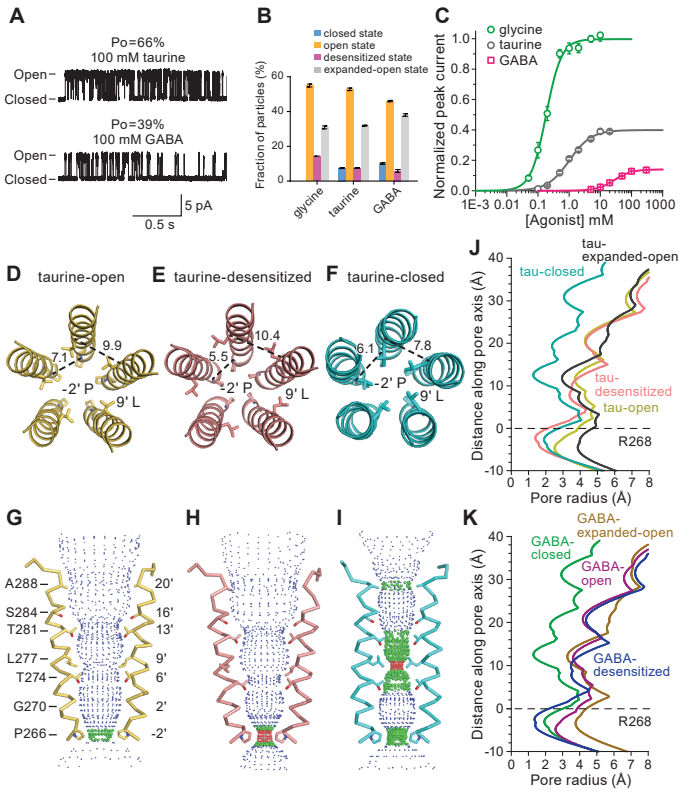

Figure 2

Figure. 3

Click here to access/download;Figure;Figure3.pdf

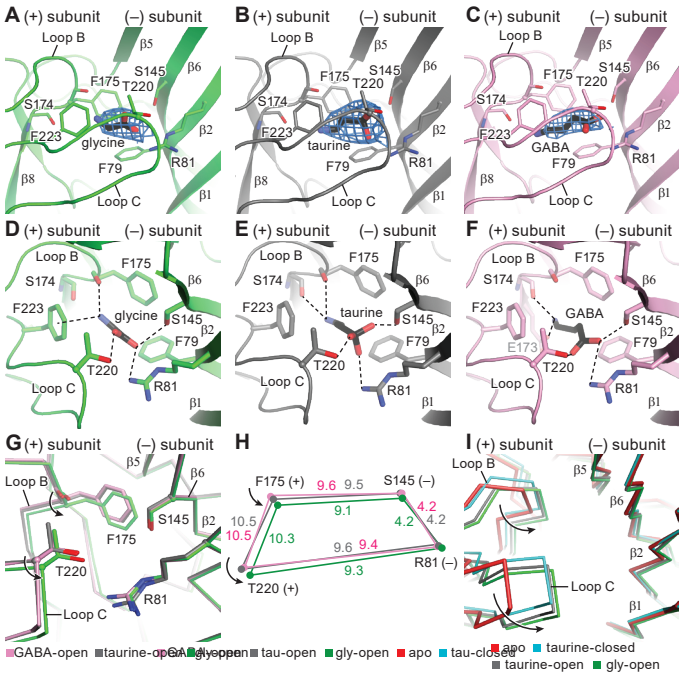

Figure 3

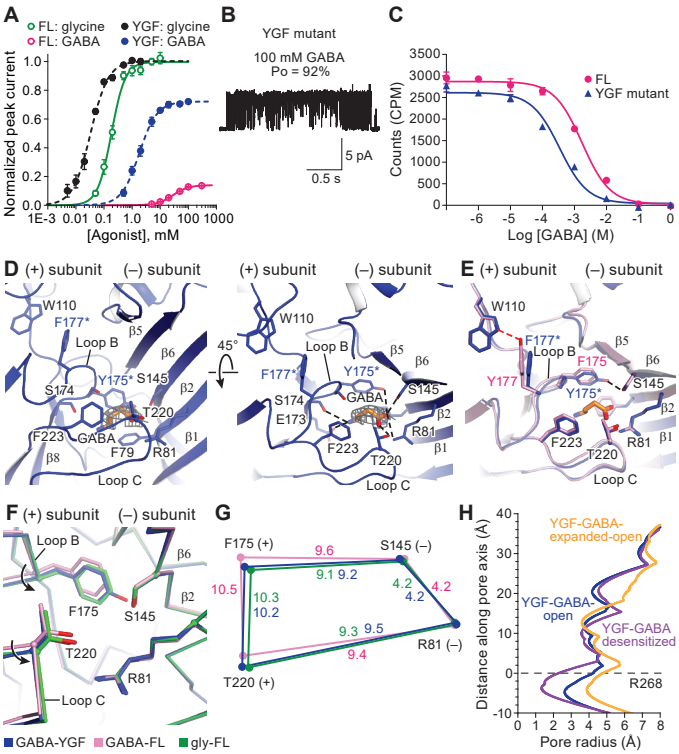

Figure 4

Figure. 5

Click here to access/download;Figure;Figure5.pdf

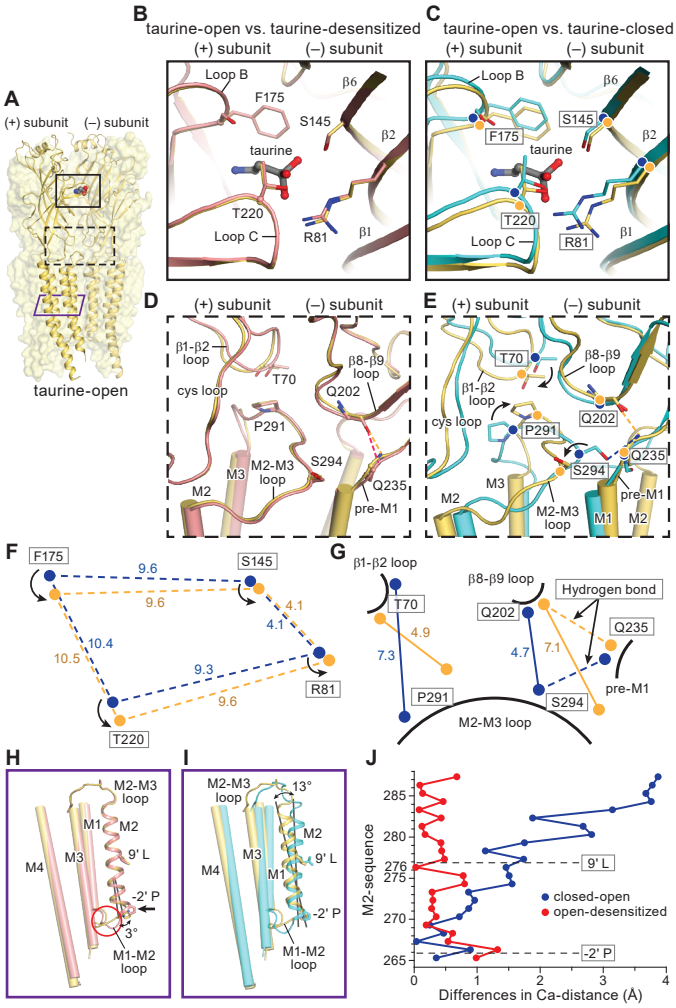

Figure 5

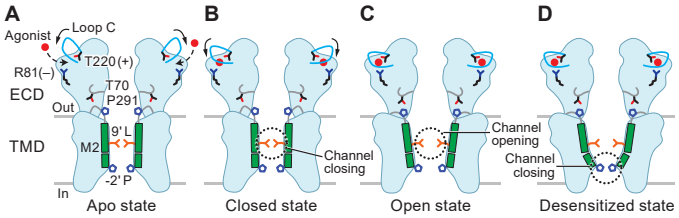

Figure 6

Supplemental Information

GlyR reconstituted into nanodisc

We also reconstituted the detergent purified receptor into nanodiscs in the presence of saturating solutions of glycine, taurine or GABA. For the full agonist (glycine), the cryo-EM data set yielded a reconstruction (GlyR-nanodisc-gly) with a single 3D class at 3.2 Å resolution (Figures S1C-S1D, S5 and S7, Table S1). The receptor features are well resolved and there is clear density for lipids and the membrane scaffold protein (MSP). Within the receptor transmembrane domain (TMD), at the 9'L and -2'P constriction sites on the M2 helix, the pore has a radius of 4 Å and 1.5 Å, respectively, suggesting that the 9'L gate is 'open' and the -2'P gate is closed, consistent with the receptor occupying a desensitized-like conformation (Figure 1C, Figure S1C-S1D).

For each partial agonist taurine and GABA, three-dimensional classification of the nanodisc cryo-EM data sets, reveals 2 distinct classes, respectively, with overall resolutions of 2.8 to 3.3 Å and local resolutions as high as 2.5 Å in the extracellular domain (ECD) (Figures S6-S8, Tables S1 and S5). One of the two structures is reminiscent of the glycine-bound desensitized state. Another one is partial agonist-bound closed state with M2 helices are approximately perpendicular to the membrane, similar as the closed state observed in the SMA data sets (Figure S1F-S1H). We did not observe the open and super-open states as in the nanodisc data sets. Because we did not observe any open states in the nanodisc-derived cryo-EM data sets, we focused our attention on the SMA-isolated receptor.

Table S1 | Statistics for 3D reconstruction and model refinement in the nanodisc. Related to Figures 1 and 2.

Ligand **State**	**Glycine** Desensitized (EMD-20373) (PDB 6PLR)	**Taurine** Desensitized (EMD-20374) (PDB 6PLS)	**Taurine** Closed (EMD-20375) (PDB 6PLT)	**GABA** Desensitized (EMD-20376) (PDB 6PLU)	**GABA** Closed (EMD-20377) (PDB 6PLV)
Data collection and processing					
Microscope	Arctica Talos	Arctica Talos	Arctica Talos	Arctica Talos	Arctica Talos
Camera	K2 Summit	K2 Summit	K2 Summit	K2 Summit	K2 Summit
Magnification	45,000	45,000	45,000	45,000	45,000
Voltage (kV)	200	200	200	200	200
Defocus range (μm)	-0.8 to -2.2	-0.8 to -2.2	-0.8 to -2.2	-0.8 to -2.2	-0.8 to -2.2
Exposure time (s)	10	10	10	10	10
Dose rate (e^-/Å^2/s)	6.1	6.1	6.1	6.1	6.1
Number of frames (no.)	100	100	100	100	100
Pixel size (Å)	0.899	0.899	0.899	0.899	0.899
Symmetry imposed	C5	C5	C5	C5	C5
Initial particles (no.)	472910	669253	669253	493873	493873
Final particles (no.)	80121	124857	15292	39926	38383
Map resolution (Å)	3.2	3.0	3.2	3.3	3.3
FSC threshold	0.143	0.143	0.143	0.143	0.143
Map resolution range (Å)	3.0–3.4	2.7–3.9	3.1–3.9	3.0–3.8	2.9–4.1
Refinement					
Initial model (PDB code)	6PLS	3JAF	3JAD	6PLS	6PLT
Model resolution (Å)	3.3	3.0	3.3	3.3	3.4
FSC threshold	0.5	0.5	0.5	0.5	0.5
Model composition					
Non-hydrogen atoms	14685	14610	14445	14665	14655
Protein atoms	13915	13805	13935	13835	13980
Ligand atoms	770	805	510	830	675
B factors (Å^2)					
Protein	83.0	48.9	120.0	84.3	69.1
Ligand	58.7	21.1	114.2	58.7	58.6
Lipid	88.1	67.5	96.4	94.8	66.3
R.m.s. deviations					
Bond length (Å)	0.004	0.008	0.005	0.008	0.009
Bond angle (°)	0.837	1.027	0.835	0.952	0.996
Validation					
Favored (%)	95.96	97.41	96.72	97.06	97.48
Allowed (%)	4.04	2.59	3.28	2.94	2.52
Disallowed (%)	0	0	0	0	0
Poor rotamers (%)	0	0	0	0	0
MolProbity score	1.46	1.40	1.56	1.50	1.57
Clash score	4.26	5.21	4.00	5.55	4.11

Table S2 | Statistics for 3D reconstruction and model refinement of glycine and taurine bound GlyR in the SMA. Related to Figures 1 and 2.

Ligand **State**	**Glycine** Desensitized (EMD-20388) (PDB 6PM5)	**Glycine** Open (EMD-20389) (PDB 6PM6)	**Glycine** Expanded-open (EMD-20386) (PDB 6PM4)	**Taurine** Desensitized (EMD-20383) (PDB 6PM1)	**Taurine** Open (EMD-20384) (PDB 6PM2)	**Taurine** Expanded-open (EMD-20382) (PDB 6PM0)	**Taurine** Closed (EMD-20385) (PDB 6PM3)
Data collection and processing							
Microscope	Titan Krios	Titan Krios	Titan Krios	Titan Krios	Titan Krios	Titan Krios	Titan Krios
Camera	K2 Summit	K2 Summit	K2 Summit	K2 Summit	K2 Summit	K2 Summit	K2 Summit
Magnification	165,000	165,000	165,000	165,000	165,000	165,000	165,000
Voltage (kV)	300	300	300	300	300	300	300
Defocus range (μm)	-1.0 to -2.0	-1.0 to -2.0	-1.0 to -2.0	-1.0 to -2.0	-1.0 to -2.0	-1.0 to -2.0	-1.0 to -2.0
Exposure time (s)	8	8	8	8	8	8	8
Dose rate (e^-/Å^2/s)	5.1	5.1	5.1	5.1	5.1	5.1	5.1
Number of frames (no.)	40	40	40	40	40	40	40
Pixel size (Å)	0.823	0.823	0.823	0.823	0.823	0.823	0.823
Symmetry imposed	C5	C5	C5	C5	C5	C5	C5
Initial particles (no.)	1578324	1578324	1578324	1124737	1124737	1124737	1124737
Final particles (no.)	39586	155456	84978	17271	122322	74365	17873
Map resolution (Å)	3.1	2.9	4.0	3.0	2.8	3.1	3.0
FSC threshold	0.143	0.143	0.143	0.143	0.143	0.143	0.143
Map resolution range (Å)	2.5–4.4	2.5–4.5	3.4–5.5	2.5–4.0	2.5–4.5	2.7–4.3	2.7–3.9
Refinement							
Initial model (PDB code)	6PLS	6PM5	6PM5	6PLS	6PM5	6PM5	6PLT
Model resolution	3.2	3.1	4.2	3.0	3.2	3.1	3.2
FSC threshold	0.5	0.5	0.5	0.5	0.5	0.5	0.5
Model composition							
Non-hydrogen atoms	14150	14100	14055	14160	14125	14080	14120
Protein atoms	13890	13840	13835	13930	13895	13850	13945
Ligand atoms	260	260	220	230	230	230	175
B factors (Å^2)							
Protein	97.8	101.4	242.1	94.1	98.7	111.5	48.8
Ligand	87.0	80.7	-	68.9	79.8	69.0	35.0
R.m.s. deviations							
Bond length (Å)	0.001	0.005	0.007	0.007	0.008	0.007	0.005
Bond angle (°)	0.399	0.911	0.927	0.954	1.021	0.968	0.916
Validation							
Favored (%)	97.66	95.96	90.12	96.49	95.61	95.91	96.95
Allowed (%)	2.34	4.04	9.88	3.51	4.39	4.09	3.05
Disallowed (%)	0	0	0	0	0	0	0
Poor rotamers	0	0	0	0	0	0	0
MolProbity score	1.35	1.61	1.97	1.63	1.52	1.55	1.58
Clash score	5.03	5.13	7.69	5.69	4.47	5.03	4.67

Table S3 | Statistics for 3D reconstruction and model refinement of the GABA bound GlyR in the SMA. Related to Figure 2.

Ligand **State**	**GABA** Desensitized (EMD-20379) (PDB 6PLX)	**GABA** Open (EMD-20380) (PDB 6PLY)	**GABA** Expanded-open (EMD-20378) (PDB 6PLW)	**GABA** Closed (EMD-20381) (PDB 6PLZ)
Data collection and processing				
Microscope	Titan Krios	Titan Krios	Titan Krios	Titan Krios
Camera	K2 Summit	K2 Summit	K2 Summit	K2 Summit
Magnification	165,000	165,000	165,000	165,000
Voltage (kV)	300	300	300	300
Defocus range (μm)	-1.0 to -2.0	-1.0 to -2.0	-1.0 to -2.0	-1.0 to -2.0
Exposure time (s)	8	8	8	8
Dose rate (e^-/Å^2/s)	5.1	5.1	5.1	5.1
Number of frames	40	40	40	40
Pixel size (Å)	0.823	0.823	0.823	0.823
Symmetry imposed	C5	C5	C5	C5
Initial particles (no.)	2062519	2062519	2062519	2062519
Final particles (no.)	20845	150199	121470	31667
Map resolution (Å)	2.9	2.9	3.0	3.0
FSC threshold	0.143	0.143	0.143	0.143
Map resolution range (Å)	2.6–4.2	2.7–4.3	2.7–4.3	2.6–4.2
Refinement				
Initial model (PDB code)	6PLS	6PM5	6PM5	6PLT
Model resolution (Å)	3.1	3.1	3.1	3.3
FSC threshold	0.5	0.5	0.5	0.5
Model composition				
Non-hydrogen atoms	14240	14165	14095	14210
Protein atoms	13970	13935	13865	13980
Ligand atoms	270	230	230	230
B factors (Å^2)				
Protein	110.6	127.2	139.3	92.0
Ligand	151.0	107.5	104.6	90.1
R.m.s. deviations				
Bond length (Å)	0.006	0.005	0.010	0.006
Bond angle (°)	0.953	0.865	0.965	0.929
Validation				
Favored (%)	96.20	94.91	96.49	96.01
Allowed (%)	3.80	5.09	3.51	3.99
Disallowed (%)	0	0	0	0
Poor rotamers	0	0	0	0
MolProbity score	1.53	1.62	1.50	1.59
Clash score	6.04	5.12	5.06	4.54

Table S4 | Statistics for 3D reconstruction and model refinement of YGF mutant and apo-GlyR$_{EM}$ in the micelle. Related to Figure 4.

Ligand **State**	**GABA** Open (EMD-20370) (PDB 6PLO)	**GABA** Expanded-open (EMD-20372) (PDB 6PLQ)	**GABA** Desensitized (EMD-20371) (PDB 6PLP)	**-** Apo-GlyR$_{EM}$ (EMD-20518) (PDB 6PXD)
Data collection and processing				
Microscope	Titan Krios	Titan Krios	Titan Krios	Titan Krios
Camera	K3 BioQuantum	K3 BioQuantum	K3 BioQuantum	K2 Summit
Magnification	130,000	130,000	130,000	130,000
Voltage (kV)	300	300	300	300
Defocus range (μm)	-1.0 to -2.0	-1.0 to -2.0	-1.0 to -2.0	-1.2 to -2.5
Exposure time (s)	1.5	1.5	1.5	6
Dose rate (e^-/Å^2/s)	18.8	18.8	18.8	9.2
Number of frames	60	60	60	30
Pixel size (Å)	0.648	0.648	0.648	1.040
Symmetry imposed	C5	C5	C5	C5
Initial particles (no.)	1808565	1808565	1808565	204323
Final particles (no.)	32386	42097	27496	115864
Map resolution (Å)	3.3	3.4	3.3	2.9
FSC threshold	0.143	0.143	0.143	0.143
Map resolution range (Å)	3.2–4.4	3.0–4.1	3.1–4.3	2.4–3.7
Refinement				
Initial model (PDB code)	6PLY	6PLW	6PLX	3JAD
Model resolution (Å)	3.4	3.5	3.4	3.2
FSC threshold	0.5	0.5	0.5	0.5
Model composition				
Non-hydrogen atoms	14165	14110	14240	13760
Protein atoms	13935	13880	14010	1616
Ligand atoms	230	230	230	144
B factors (Å^2)				
Protein	131.6	150.6	109.8	69.4
Ligand	116.7	131.7	94.0	-
R.m.s. deviations				
Bond length (Å)	0.007	0.007	0.001	0.007
Bond angle (°)	0.999	0.977	0.416	1.30
Validation				
Favored (%)	95.44	94.91	97.95	95.27
Allowed (%)	4.56	5.09	2.05	4.73
Disallowed (%)	0	0	0	0
Poor rotamers	0	0	0	1.32
MolProbity score	1.34	1.46	1.65	1.99
Clash score	6.08	3.13	6.08	11.24

Table S5 | Resolution summary for all the maps. Related to Figures 1-2 and 4.

Membrane mimic	Agonist	State	Resolution (Å)
MSP-lipid nanodisc	glycine	Desensitized	3.2
	taurine	Desensitized	3.0
		Closed	3.2
	GABA	Desensitized	3.3
		Closed	3.3
SMA	glycine	Open	2.9
		Desensitized	3.1
		Expanded-open	4.0
	taurine	Closed	3.0
		Open	2.8
		Desensitized	3.0
		Expanded-open	3.1
	GABA	Closed	3.0
		Open	2.9
		Desensitized	2.9
		Expanded-open	3.0
	YGF-GABA	Open	3.3
		Expanded-open	3.4
		Desensitized	3.3
Micelle	-	Apo-$GlyR_{EM}$	2.9

Table S6 | Binding pocket metrics for Cys-loop family.† Related to Figure 3.

	d_x (Å)	V_{ligand} (Å^3)	$D_{F175\text{-}S145}$ (Å)	$D_{T220\text{-}R81}$ (Å)	
Glycine receptor					
Glycine (6PM6)	2.7	53.1	9.1	9.3	Full Agonist
Taurine (6PM2)	3.5	79.0	9.5	9.4	Partial Agonist
GABA (6PLY)	4.1	86.5	9.6	9.6	Partial Agonist
Strychnine (3JAD)	3.1	258.4	10.4	12.1	Antagonist
Apo (5WP7)			10.0	12.6	
Efficacy: glycine > taurine > GABA > strychnine					
Nicotinic acetylcholine receptor					
Nicotine (5KXI) (Morales-Perez et al., 2016)	2.2*	137	9.4	9.8	Partial Agonist
AT-1001 (6PV8) (Gharpure et al., 2019)	2.0	213	13.9	12.2	Partial Agonist
Efficacy: Nicotine > AT-1001					
5HT3 receptor					
5HT (6HIO) (Polovinkin et al., 2018)	2.3	138.6	7.4	13.4	Full Agonist
Tropisetron (6HIS) (Polovinkin et al., 2018)	2.1	221.0	8.1	15.6	Antagonist
Apo (6BE1) (Basak et al., 2018)			8.6	15.7	
Efficacy: Serotonin > Tropisetron					
GABAA receptor					
GABA (6DW0) (Phulera et al., 2018)	3.7	86.5	9.3	12.0	Full Agonist
BCC (6HUK) (Masiulis et al., 2019)	3.2	263.5	10.1	12.2	Antagonist
Efficacy: GABA > BCC					

* values are obtained by Tripathy et al.(Tripathy et al., 2019).

† Four measurements are performed for each structure: 1) the d_x (in Å) as defined by Auerbach and colleagues(Tripathy et al., 2019); 2) the volume of ligand (V_{ligand}; in Å^3) calculated using the Molecular Volume Calculator(Jayaram et al., 2012); 3) the distance between the Cα atoms of T175 (+) and S145 (-) ($D_{F175\text{-}S145}$; in Å) in GlyR or the corresponding Cα atoms in the non-GlyR structures; 4) the distance between the Cα atoms from T220 (+) and R81 (-) ($D_{T220\text{-}R81}$; in Å) in GlyR or the corresponding Cα atoms in the non-GlyR structures. PDB codes are noted in parentheses.

References

Basak, S., Gicheru, Y., Samanta, A., Molugu, S.K., Huang, W., Fuente, M., Hughes, T., Taylor, D.J., Nieman, M.T., Moiseenkova-Bell, V.*, et al.* (2018). Cryo-EM structure of 5-HT3A receptor in its resting conformation. Nat Commun *9*, 514.

Gharpure, A., Teng, J., Zhuang, Y., Noviello, C.M., Walsh, R.M., Jr., Cabuco, R., Howard, R.J., Zaveri, N.T., Lindahl, E., and Hibbs, R.E. (2019). Agonist Selectivity and Ion Permeation in the alpha3beta4 Ganglionic Nicotinic Receptor. Neuron.

Jayaram, B., Singh, T., Mukherjee, G., Mathur, A., Shekhar, S., and Shekhar, V. (2012). Sanjeevini: a freely accessible web-server for target directed lead molecule discovery. BMC Bioinformatics *13 Suppl 17*, S7.

Masiulis, S., Desai, R., Uchanski, T., Serna Martin, I., Laverty, D., Karia, D., Malinauskas, T., Zivanov, J., Pardon, E., Kotecha, A.*, et al.* (2019). GABAA receptor signalling mechanisms revealed by structural pharmacology. Nature *565*, 454-459.

Morales-Perez, C.L., Noviello, C.M., and Hibbs, R.E. (2016). X-ray structure of the human alpha4beta2 nicotinic receptor. Nature *538*, 411-415.

Phulera, S., Zhu, H., Yu, J., Claxton, D.P., Yoder, N., Yoshioka, C., and Gouaux, E. (2018). Cryo-EM structure of the benzodiazepine-sensitive alpha1beta1gamma2S tri-heteromeric GABAA receptor in complex with GABA. Elife *7*.

Polovinkin, L., Hassaine, G., Perot, J., Neumann, E., Jensen, A.A., Lefebvre, S.N., Corringer, P.J., Neyton, J., Chipot, C., Dehez, F.*, et al.* (2018). Conformational transitions of the serotonin 5-HT3 receptor. Nature *563*, 275-279.

Tripathy, S., Zheng, W., and Auerbach, A. (2019). A single molecular distance predicts agonist binding energy in nicotinic receptors. J Gen Physiol *151*, 452-464.

Table S7 | **Fractions of each agonist-bound state as a function of image processing software. Related to Figures 1 and 2.**

Membrane mimic	**Agonists**	**States**	**Fractions (%)**		
			RELION 3.0 (Zivanov et al., 2018)	**cisTEM** (Grant et al., 2018)	**SEM**
SMA	glycine	Open	55.6	54.4	0.60
		Desensitized	14.1	14.1	0.00
		Expanded-open	30.3	31.5	0.60
	taurine	Closed	7.7	7.3	0.20
		Open	52.3	53.3	0.50
		Desensitized	7.4	7.7	0.15
		Expanded-open	32.1	31.7	0.20
	GABA	Closed	9.8	10.5	0.35
		Open	46.3	45.8	0.25
		Desensitized	6.4	5.3	0.55
		Expanded-open	37.5	38.5	0.50

References:

Zivanov, J., Nakane, T., Forsberg, B.O., Kimanius, D., Hagen, W.J., Lindahl, E., and Scheres, S.H. (2018). New tools for automated high-resolution cryo-EM structure determination in RELION-3. Elife *7*.

Grant, T., Rohou, A., and Grigorieff, N. (2018). cisTEM, user-friendly software for single-particle image processing. Elife *7*.

Figure. S1

Click here to access/download;Supplemental Figure;S1.pdf

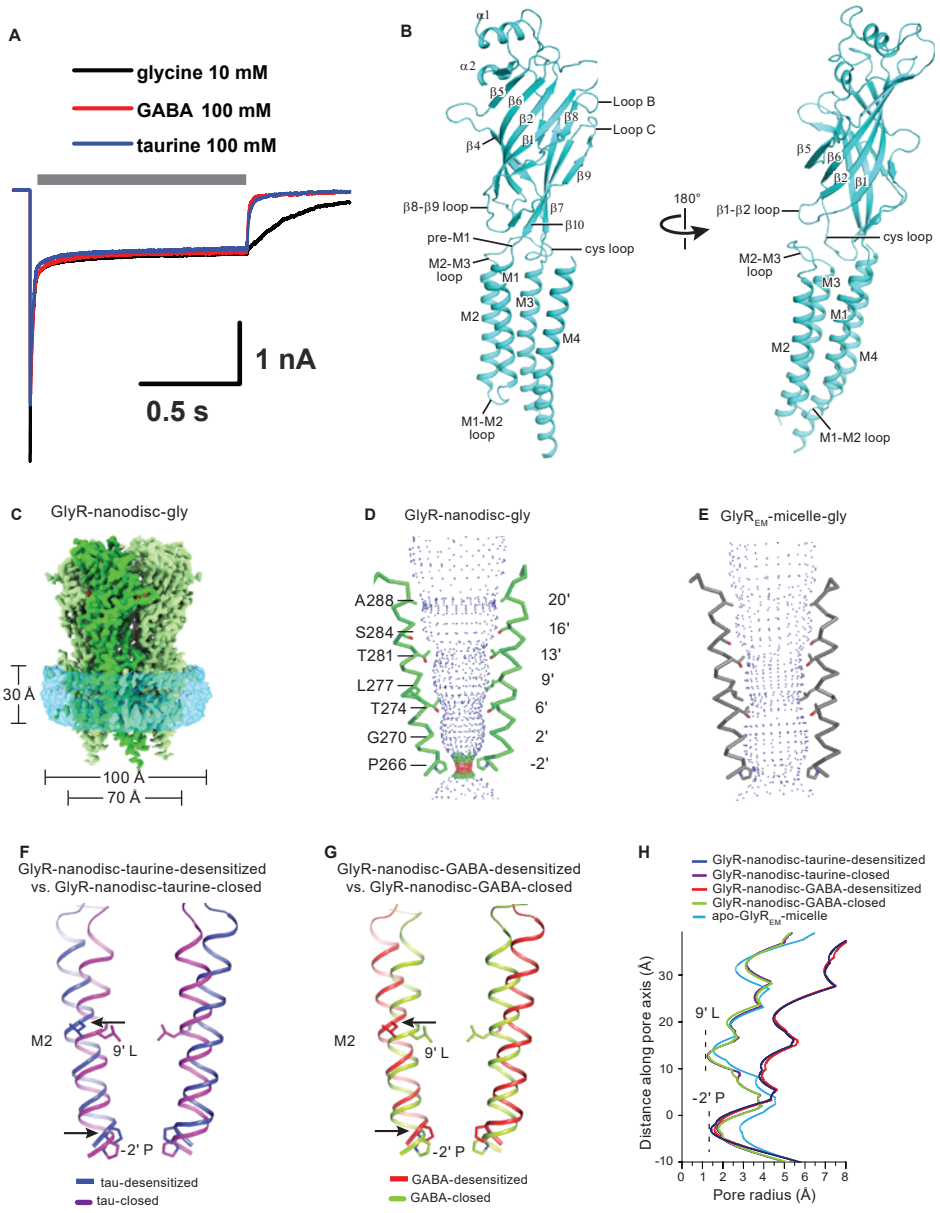

Figure S1

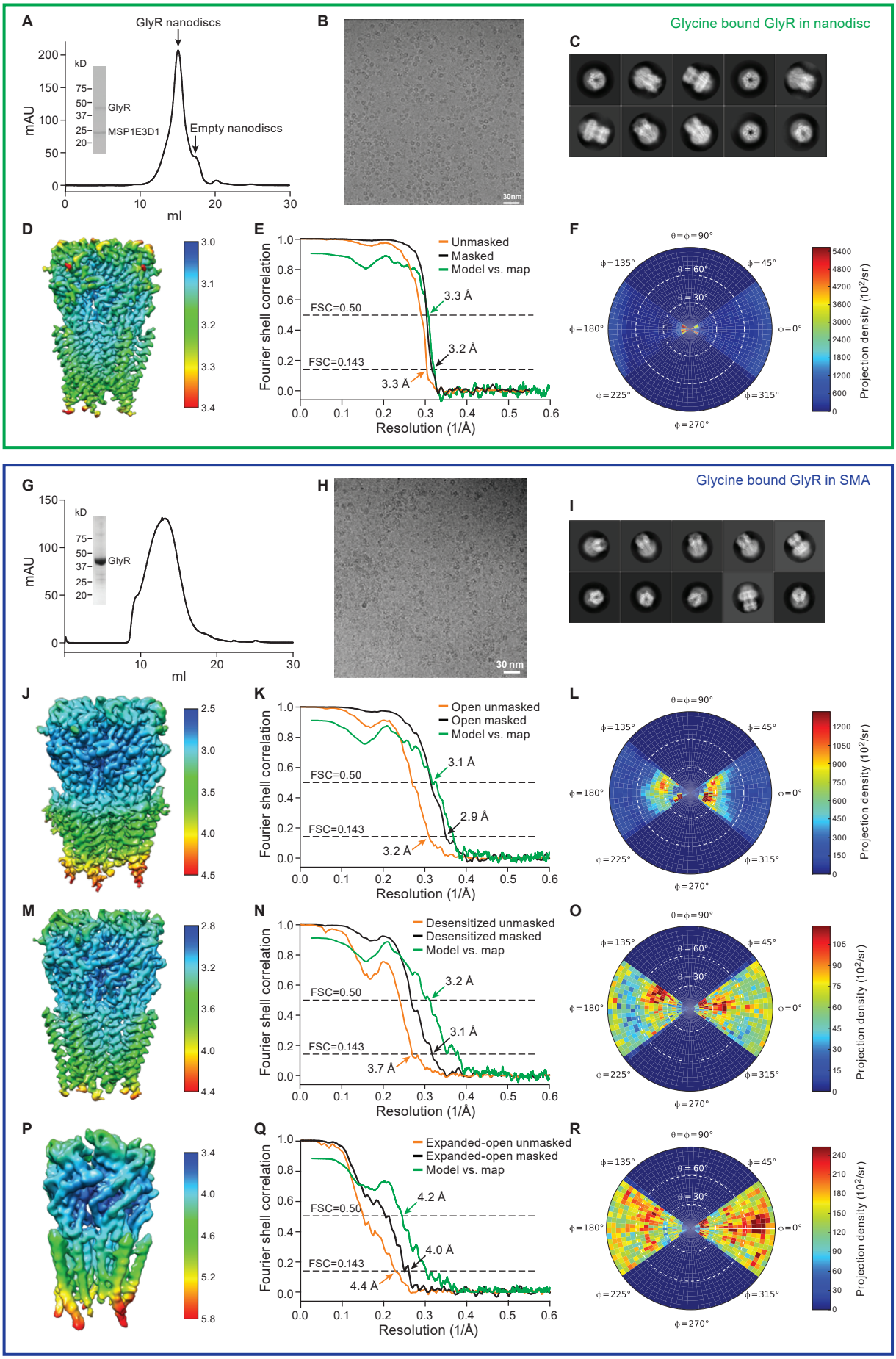

Figure S2

Figure. S3

Click here to access/download;Supplemental Figure;S3.pdf

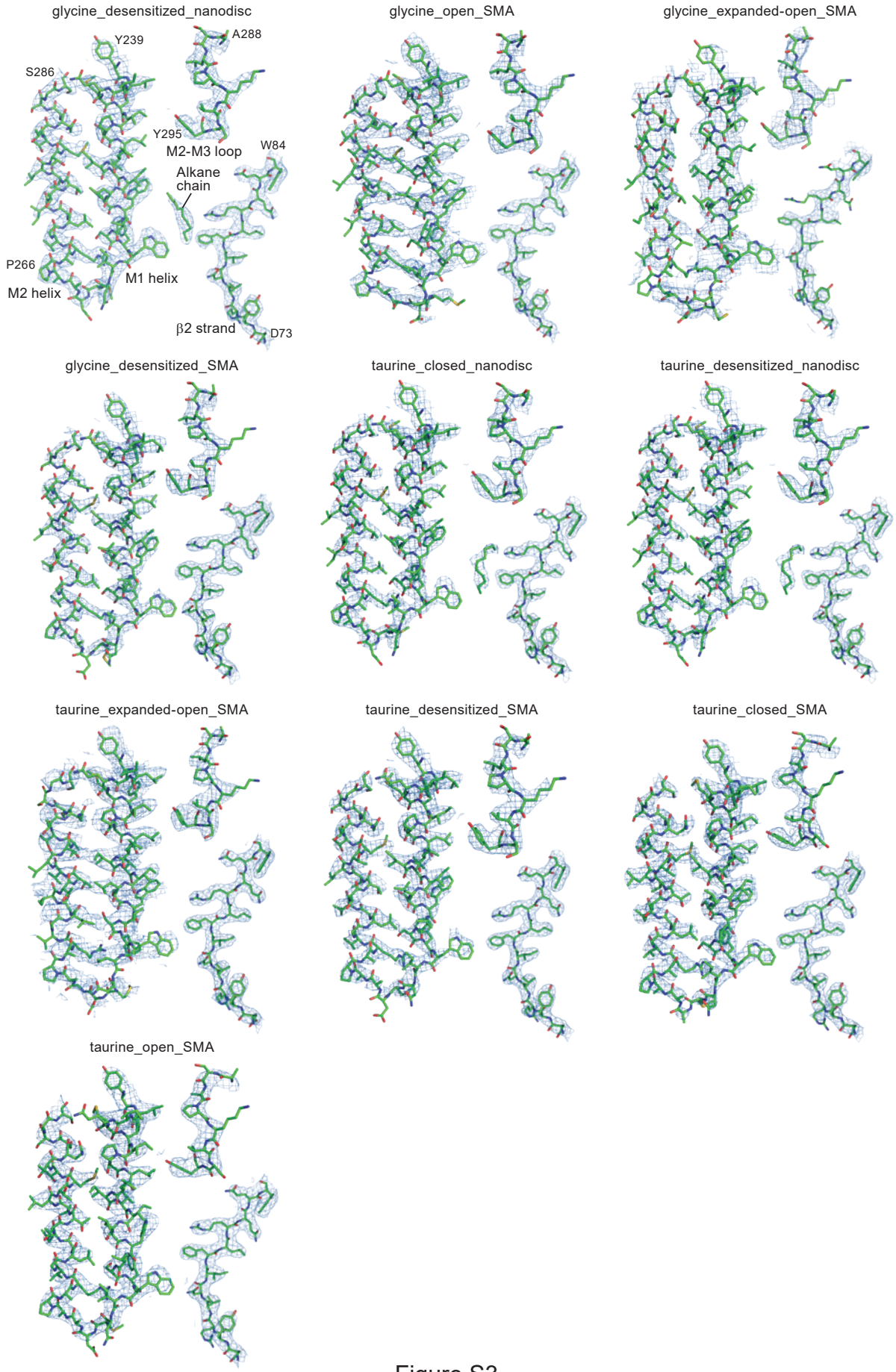

Figure S3

Figure. S4

Click here to access/download;Supplemental Figure;S4.pdf

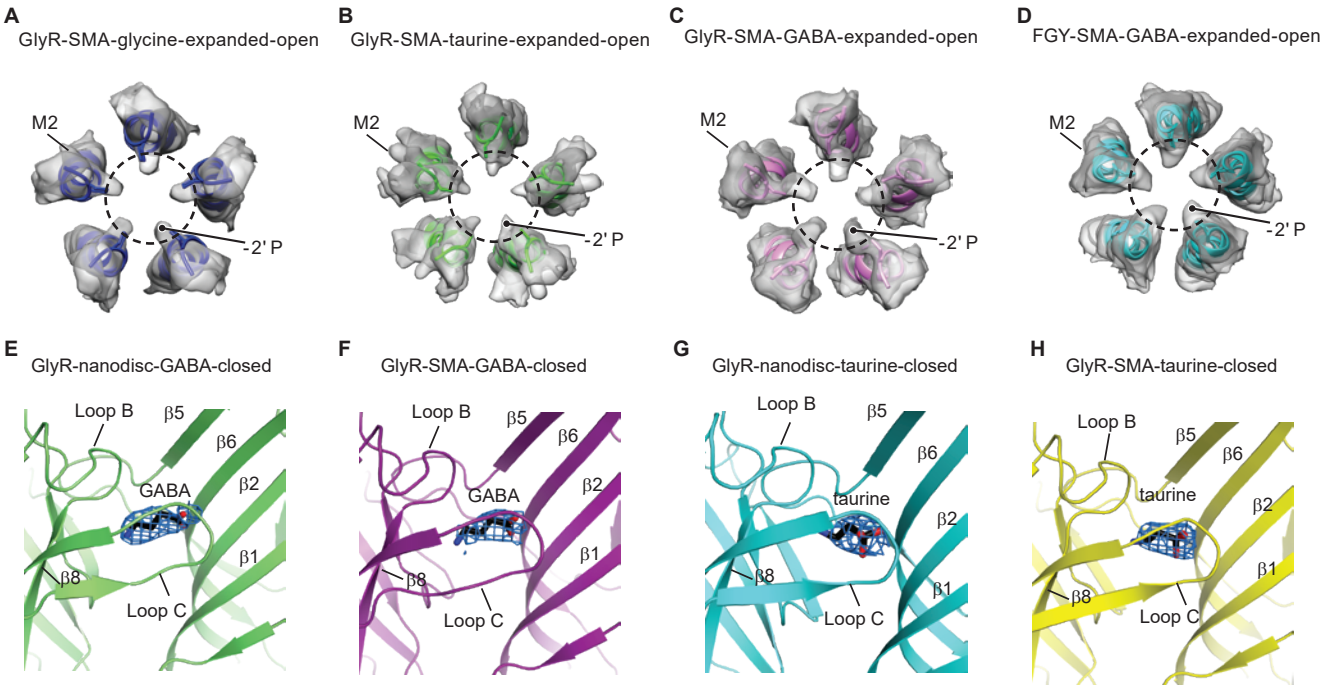

Figure S4

Figure. S5

Click here to access/download;Supplemental Figure;S5.pdf

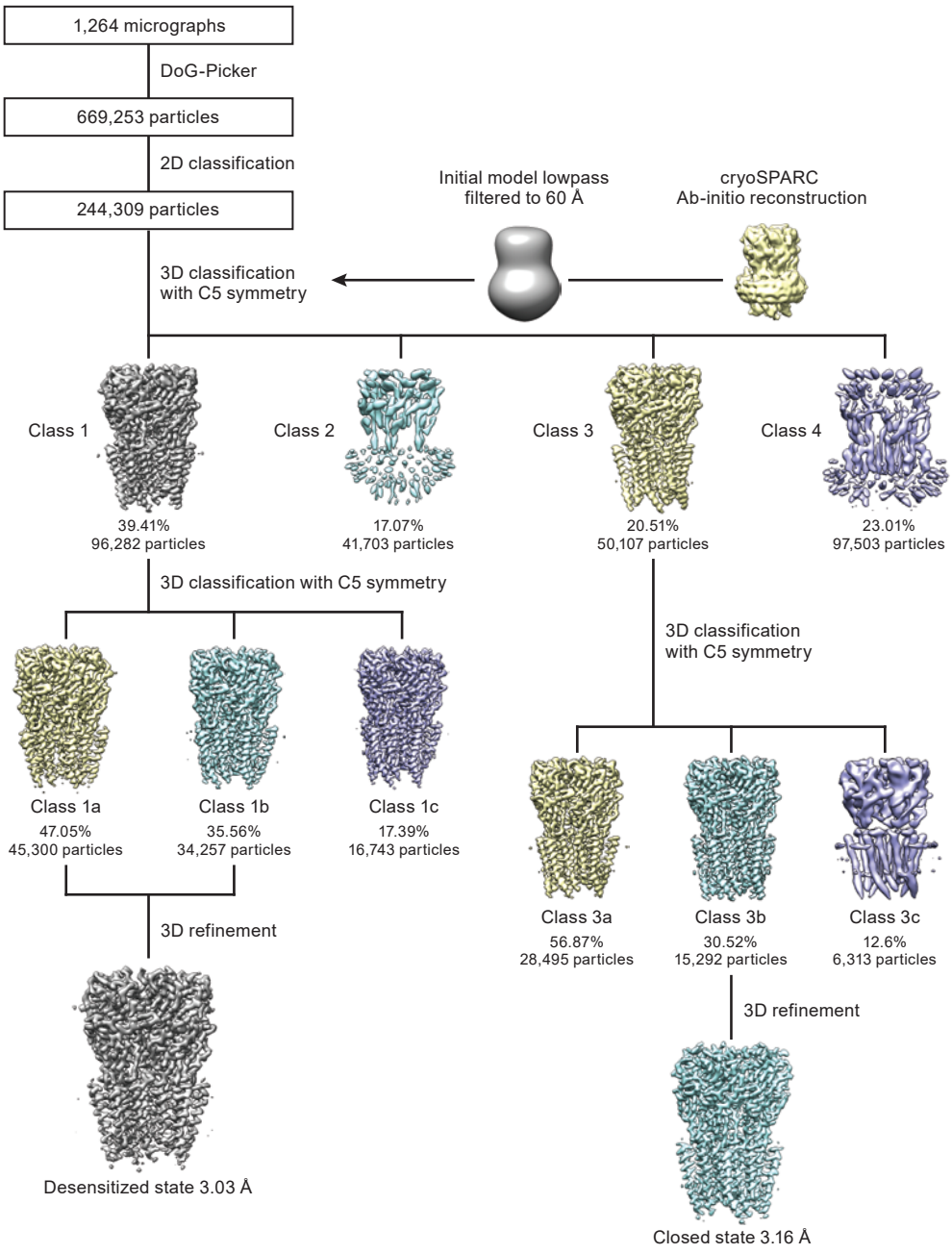

Figure S5

Figure. S6

Click here to access/download;Supplemental Figure;S6.pdf

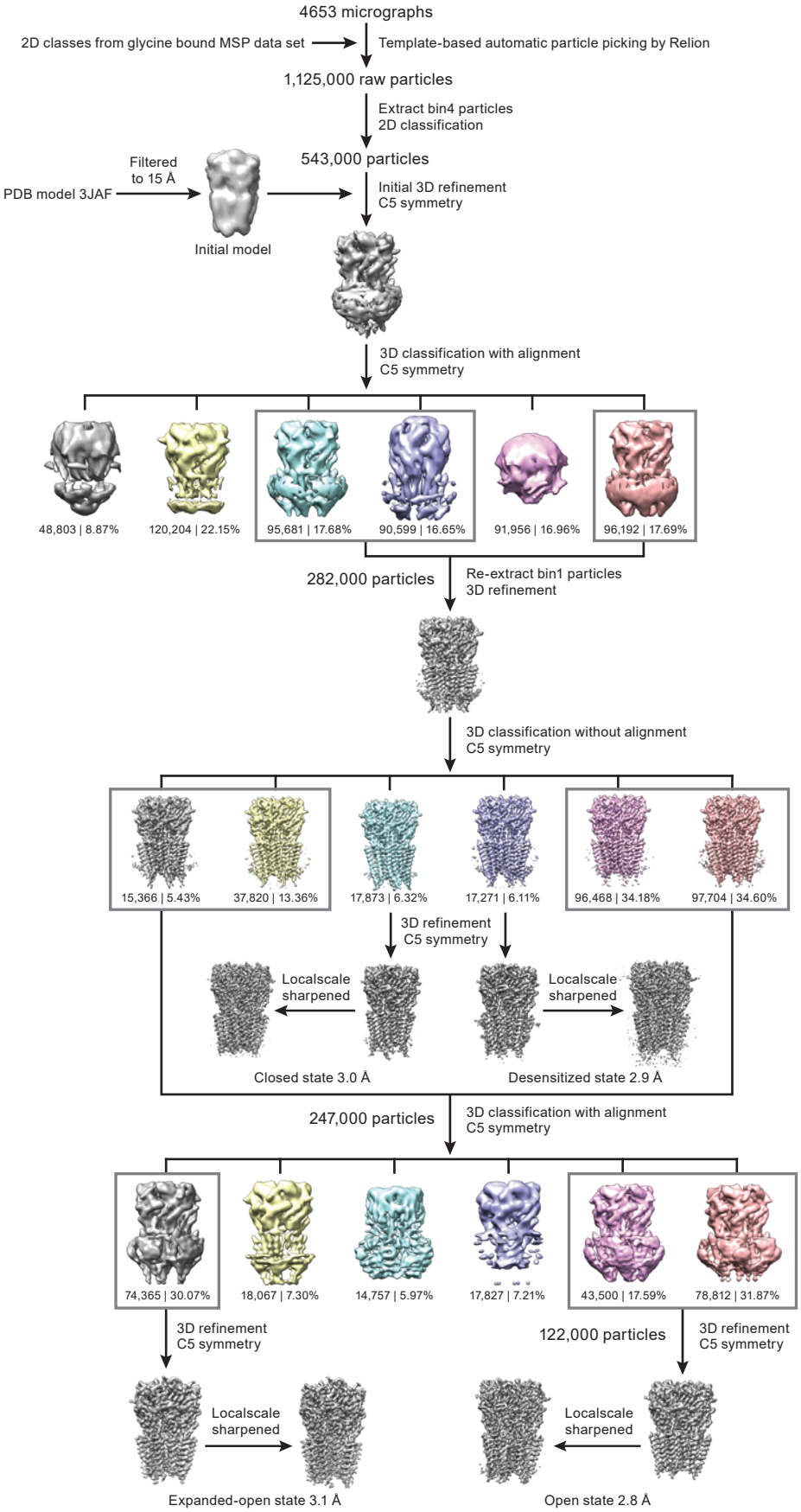

Figure S6

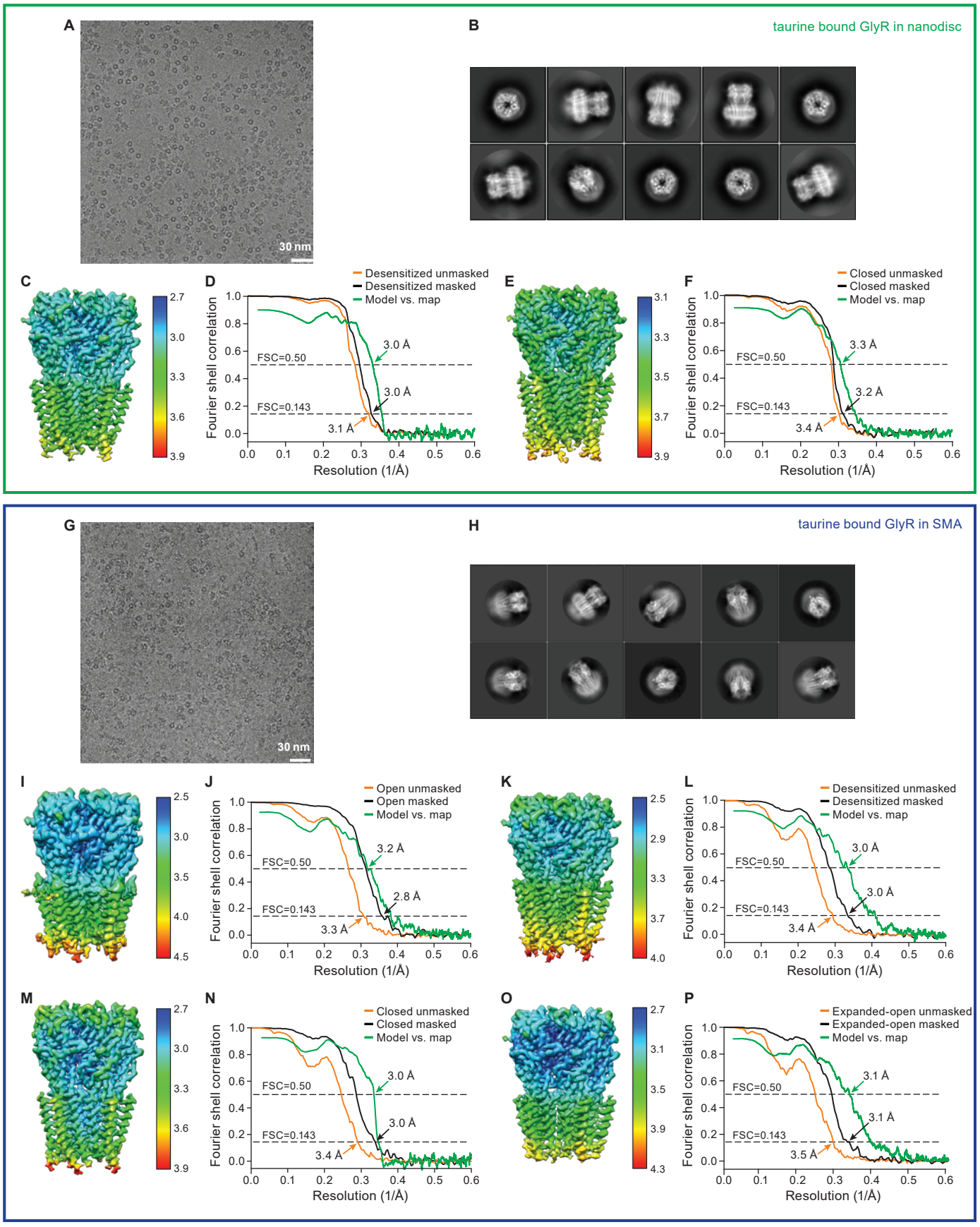

Figure S7

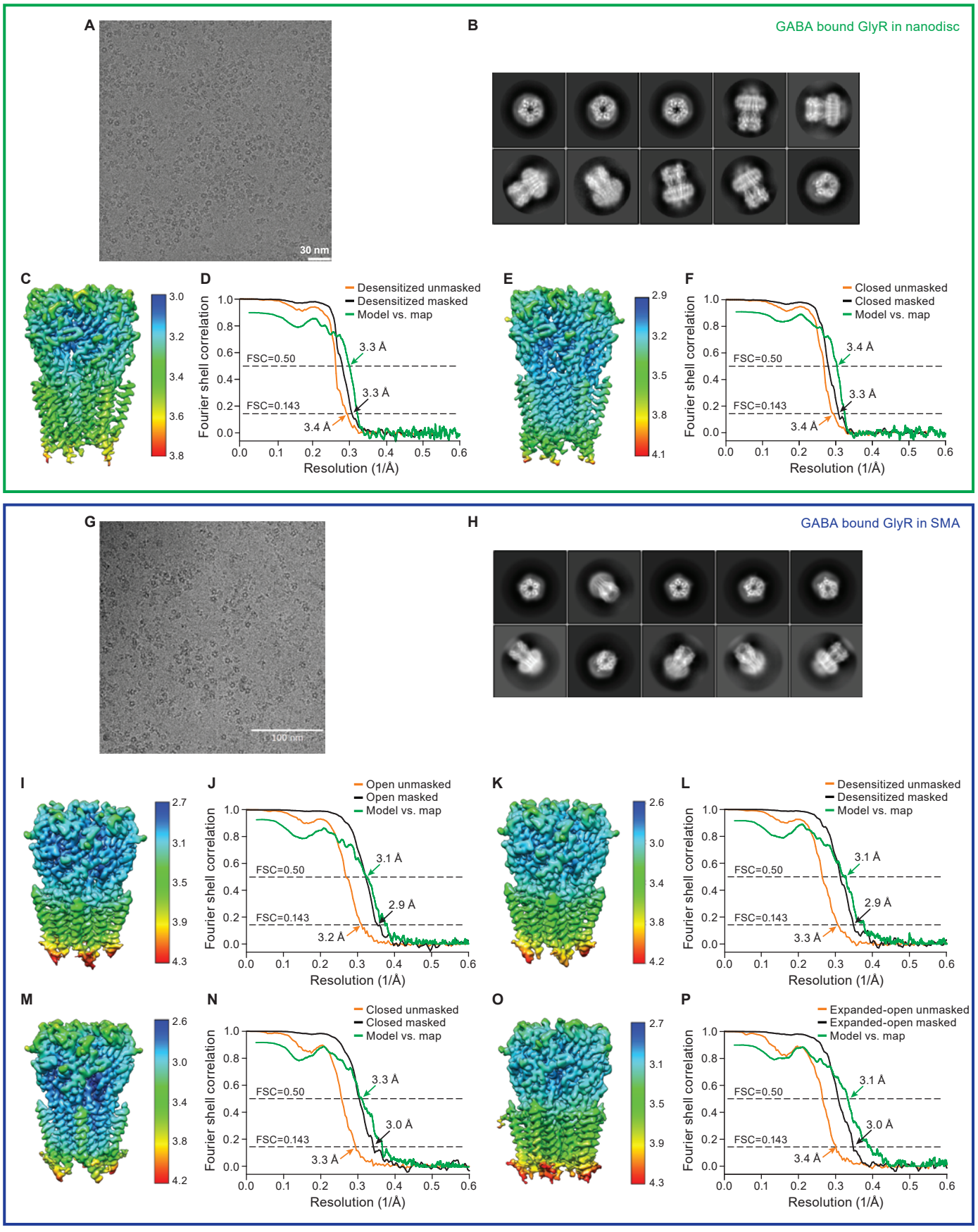

Figure S8

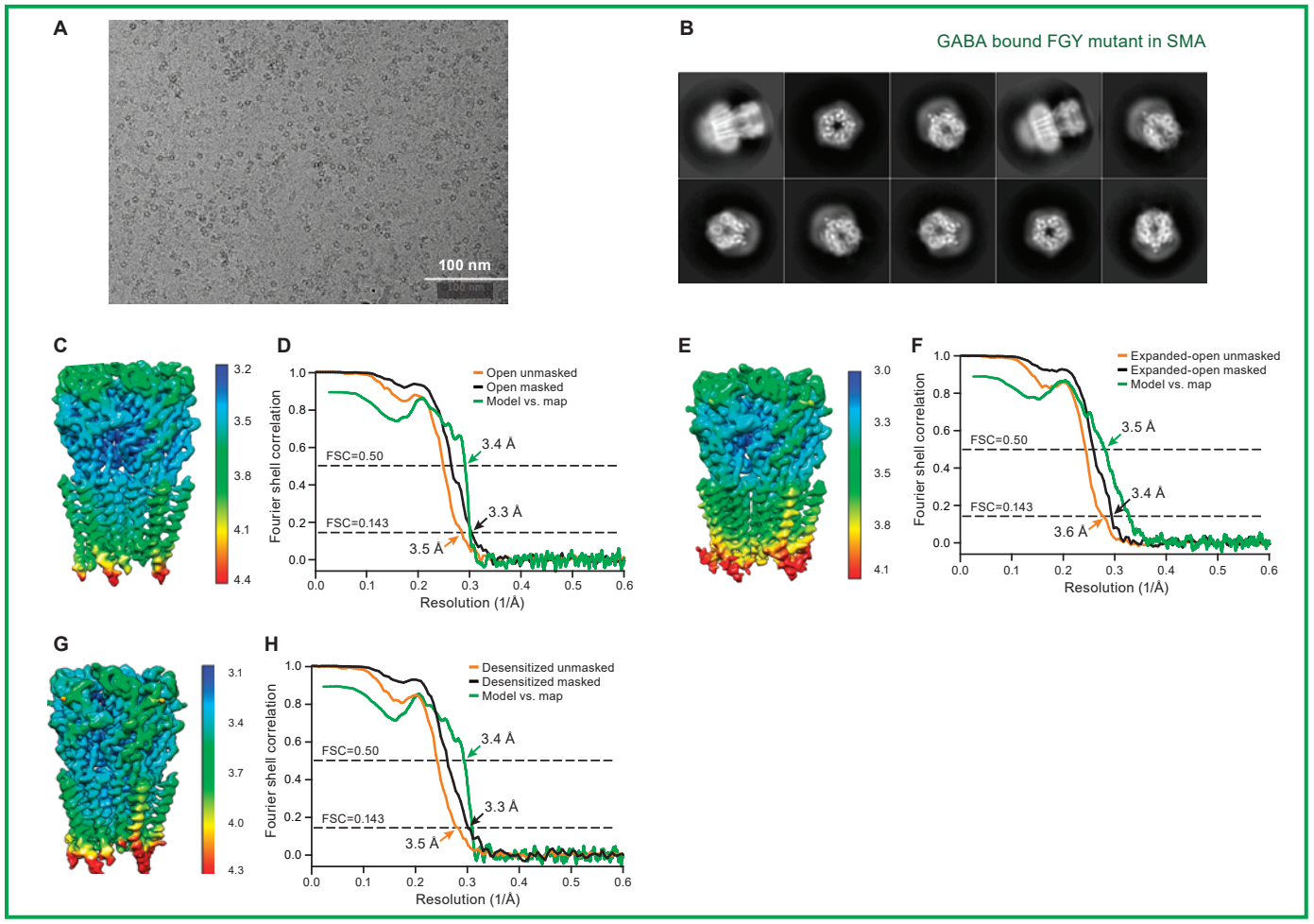

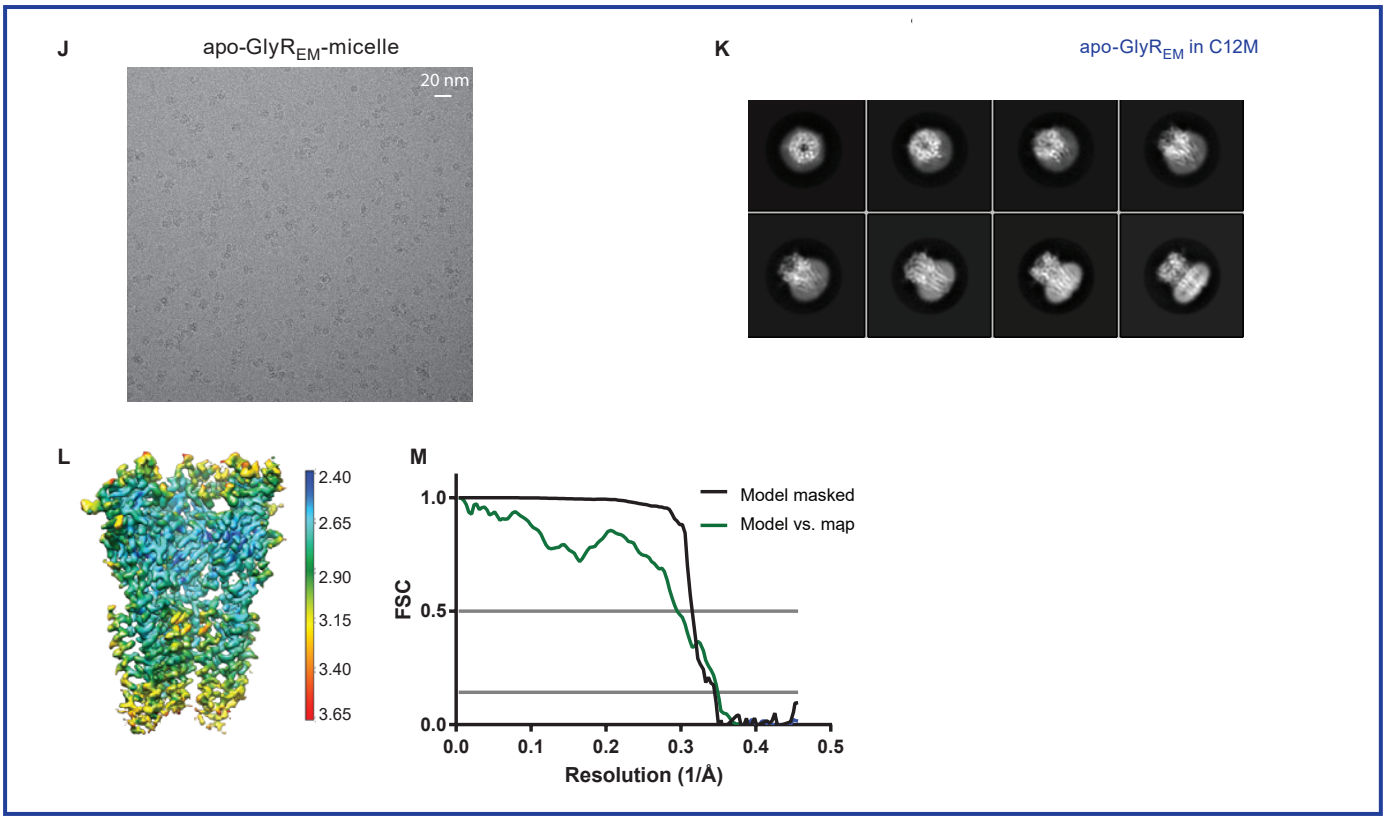

Figure S9

Figure. S10

Click here to access/download;Supplemental Figure;S10.pdf

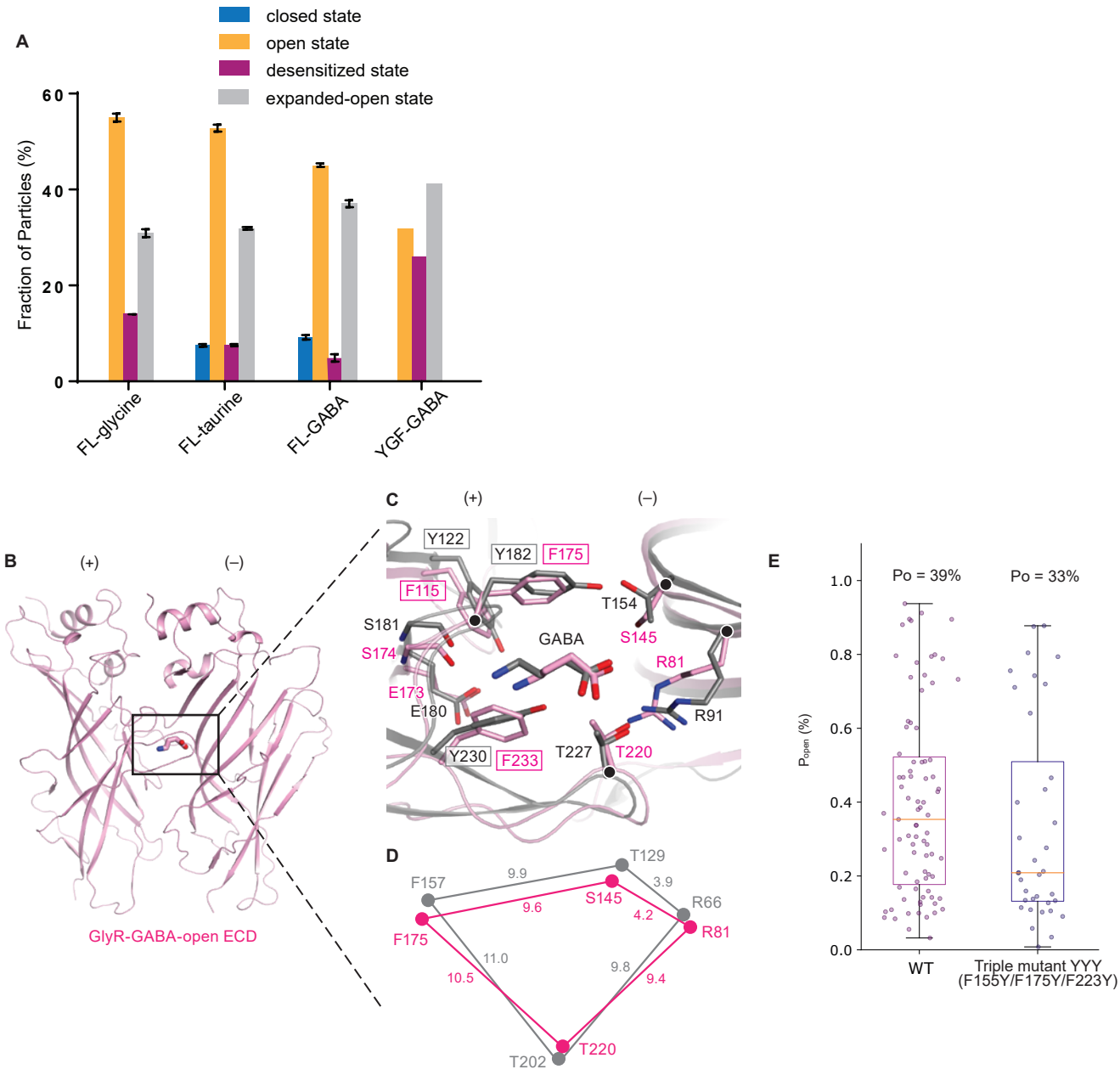

Figure S10

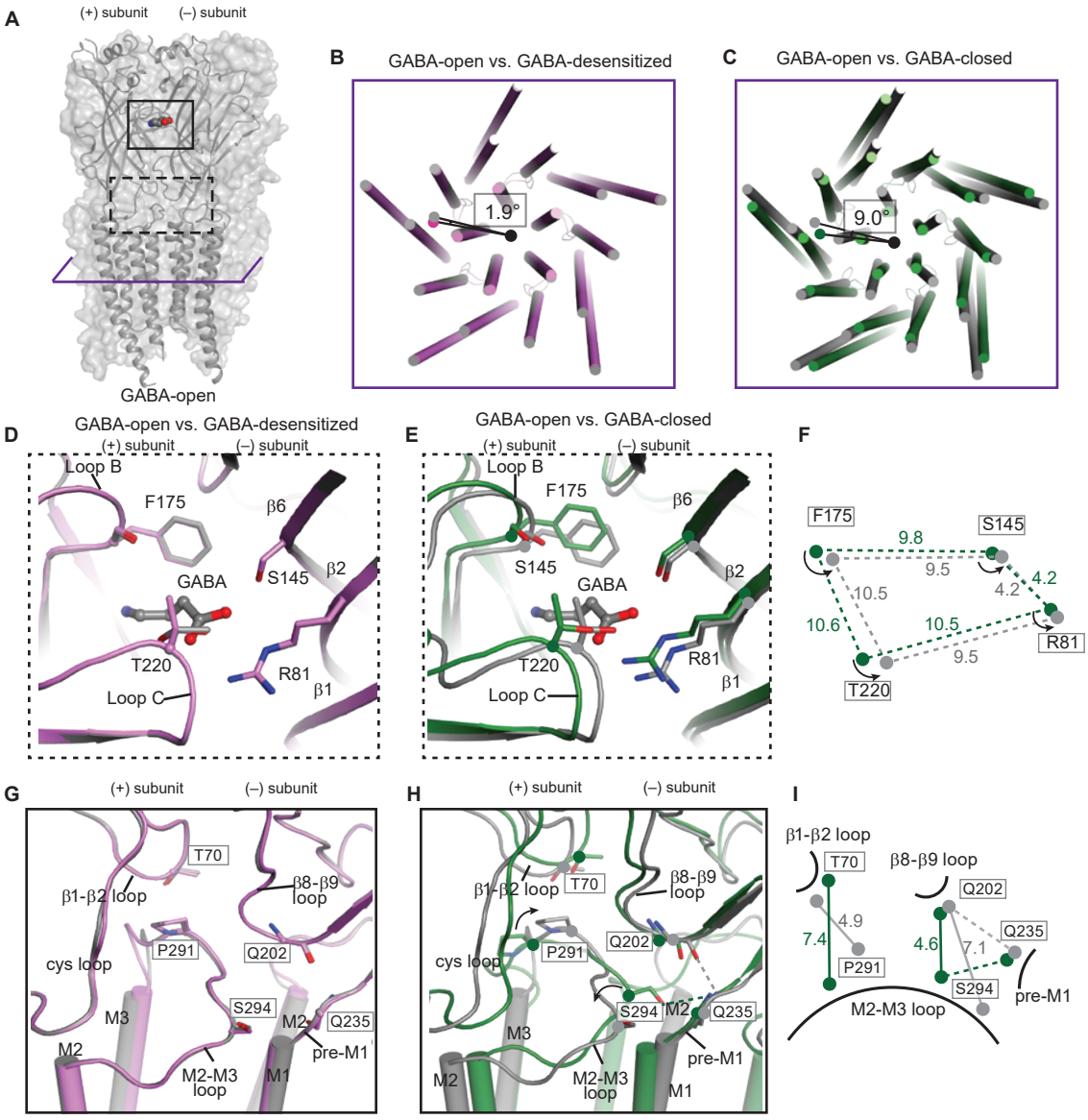
A
(+) subunit
(–) subunit
GABA-open
B
GABA-open vs. GABA-desensitized
1.9°
C
GABA-open vs. GABA-closed
9.0°
D
GABA-open vs. GABA-desensitized
(+) subunit
(–) subunit
Loop B
F175
β6
GABA
S145
β2
T220
R81
Loop C
β1
E
GABA-open vs. GABA-closed
(+) subunit
(–) subunit
Loop B
F175
β6
S145
β2
GABA
T220
R81
Loop C
β1
F
F175
S145
9.8
9.5
4.2
4.2
10.5
10.6
10.5
R81
9.5
T220
G
(+) subunit
(–) subunit
T70
β1-β2 loop
β8-β9 loop
cys loop
P291
Q202
S294
M3
M2
Q235
M2
pre-M1
M2-M3 loop
M1
H
(+) subunit
(–) subunit
β1-β2 loop
T70
β8-β9 loop
cys loop
P291
Q202
S294
M2
Q235
M3
pre-M1
M2
M2-M3 loop
M1
I
β1-β2 loop
T70
β8-β9 loop
Q202
4.9
7.4
Q235
4.6
7.1
P291
S294
pre-M1
M2-M3 loop

Figure S11

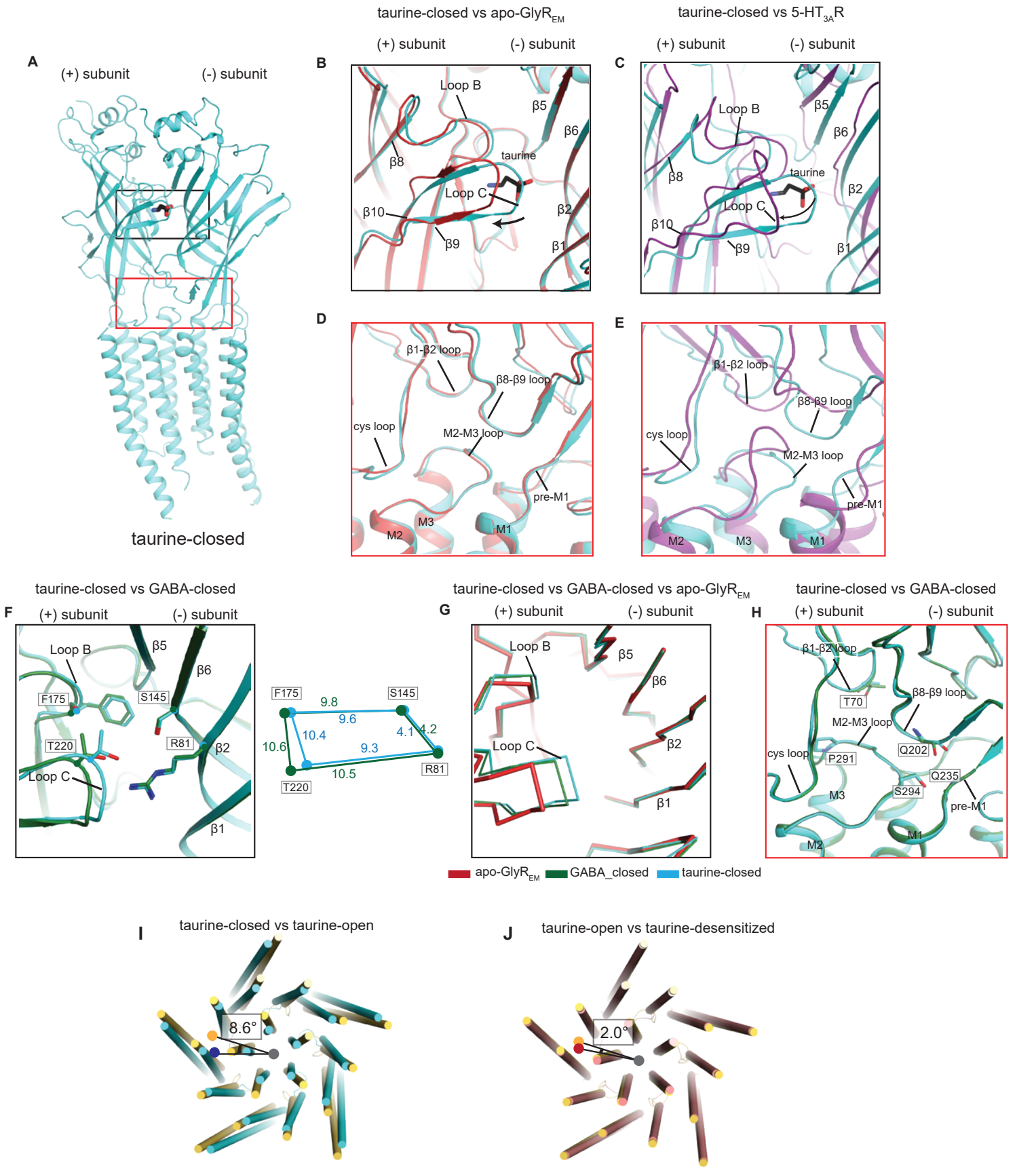

Figure S12

Figure. S13

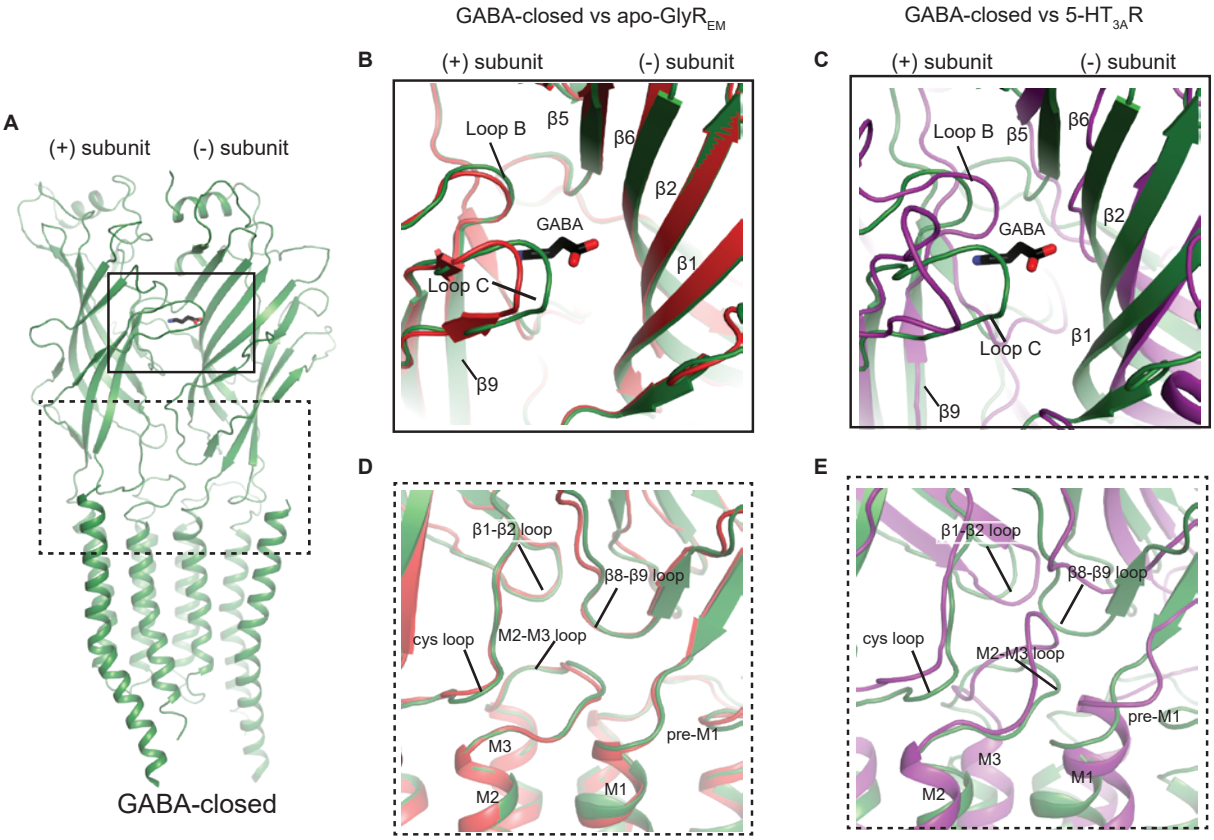

Figure S13